Review

Device architectures for photoelectrochemical water splitting based on hematite: a review

Stella Nasejje[1] · Emma Panzi Mukhokosi[1] · Mmantsae Diale[2] · Dhayalan Velauthapillai[3]

Abstract

Hydrogen production by photoelectrochemical (PEC) water splitting is a sustainable means that can avert the effects of global warming caused by fossil fuels. For decades, a suitable semiconductor that can absorb solar radiation in the visible region has been a focal research question. Hematite has a theoretical Solar-To-Hydrogen efficiency of 15% which is higher than the 10% benchmark for PEC water splitting. Despite being cheap, chemically stable, and bearing a desired band gap, hematite has not reached this projection due to challenges like band edge mismatch, short hole diffusion length and charge recombination. Various articles have shown hetero-structuring is a reliable solution to some challenges due to enhanced spectral range, enhanced carrier mobility, strong built-in electric field and thus increase in efficiency. However, these articles lack scientific rationale on the performance of hematite and its hetero-structures on different substrates, which is the basis for this review. Our analysis suggests that hetero-structure improves hematite's PEC performance due to increased spectral range, enhanced carrier mobility and built-in electric field. This review article is organized as follows: a brief PEC background, performance parameters, Physical and Crystallographic properties of hematite, device configurations, performance of hematite and its hetero-structures on different substrates.

✉ Emma Panzi Mukhokosi, epmukhokosi@kyu.ac.ug; panzi2018@gmail.com | [1]Department of Physics, Kyambogo University, Kyambogo, P. O. Box 1, Kampala, Uganda. [2]Department of Physics, University of Pretoria, Private Bag X20, Hatfield 0028, South Africa. [3]Faculty of Engineering and Science, Western Norway University of Applied Sciences, 5063 Bergen, Norway.
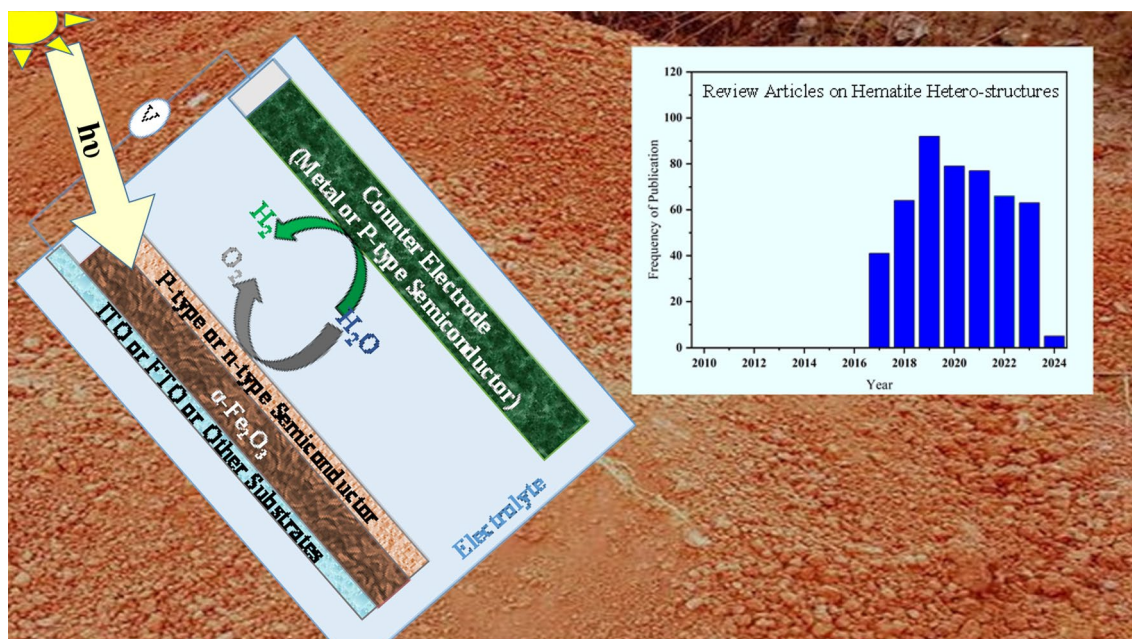
Graphical Abstract

1 Introduction

Greenhouse gases from the combustion of fossil fuels cause air pollution and climate change [1]. Green energy technology is an urgent solution required to curb the foreseen challenges associated with the use of fossil fuels [2]. Hydrogen (H_2) fuel production is projected as the best alternative to clean energy technologies if obtained by solar water splitting. Photoelectrochemical (PEC) water splitting is the most viable means of generating H_2 from solar radiation as it is sustainable, renewable, and eco-friendly [1, 3]. 43% of solar irradiation on the earth's surface is in the visible range and the need for semiconducting materials that can absorb light in this range has been a focal research question for decades [4].

For practical PEC water splitting applications, a benchmark of 10% solar-to-hydrogen (S.T.H) efficiency is required from a semiconductor photo-anode [1, 5, 6]. Hematite's theoretical S.T.H efficiency is projected at 15%, a value above the benchmarked efficiency [1, 5, 7–9]. Hematite is cheap, has a desirable band gap (~ 2.1–2.2 eV), is environmentally friendly, chemically stable in alkaline solutions, and non-toxic [2, 5, 7, 10, 11]. This has led to hematite being a focal research material for PEC applications [12–16].

However, until now, hematite has neither reached the 10% practical benchmark nor the maximum 15% efficiency. This could be due to poor electrical conductivity, the short hole-diffusion length (2–4 nm) in relation to the depth of light penetration (~ 120 nm), high photo-generated charge recombination at the surface and in the bulk due to short charge carrier life-time (~ 3–10 ps), slow oxygen evolution kinetics, inefficient separation of electron–hole pairs due to low carrier mobility (< 0.2 $cm^2V^{-1}s^{-1}$) [1–5, 7, 10] and a band edge mismatch with the redox potentials [2, 8, 17–19].

Nano-structure designs, ion doping, metal-oxide integration to form heterojunction photo-anodes, use of oxygen evolution catalysts as interfaces with hematite, forming composite structures, and surface modifications have been carried out to solve challenges concerning hematite [1–3, 7, 8, 18, 20–24].

Hematite belongs to a afamily of metal oxides and extensive work has been done to improve the performance of metal oxides for PEC devices. In this regards, song et al. assessed the PEC solar water splitting efficiency of tandem PEC cell configuration using W: $BiVO_4$/CoPi as a working photo-electrode and $CuBi_2O_4$/CdS/TiO_2/RuO_X as the counter electrode highlighting the significance of a cocatalyst in hydrogen production and photo-voltage in tandem PEC cell configurations

[25]. Other related work by the same research group focused p-$Cu_2V_2O_{10}$ and yielded a photocurrent of 0.5 mAcm^{-2}, they highlighted the importance of inserting a thin layer of Cu doped NiO between FTO substrate and CuBi2O4 photoanode which yielded a photocurrent of 2.83 mAcm^{-2}, they further developed (CuBi$_2$O$_4$/TiO$_2$/RuOx, CuBi$_2$O$_4$/CdS/TiO$_2$/RuO$_x$, CuBi$_2$O$_4$/BiVO$_4$/TiO$_2$/RuO$_x$ and CuBi$_2$O$_4$/Ga$_2$O$_3$/TiO$_2$/RuOx) heterojunctions photoelectrodes and their performance was compared based on photocurrents, band offsets, and directed charge transfer [26–29].

There are various review articles on the the performance of hematite for PEC applications. Choudhary et al. reviewed nanostructure bilayer thin films including; CdSe/CdS, TiO$_2$/CdSe/CdS, TiO$_2$/CdS, TiO$_2$/CdSe, Cu$_2$O/CuO, Cu$_2$O/ TiO$_2$, TiO$_2$/ CdTe, WO$_3$/TiO$_2$, Cu$_2$O/ZnO, BiOI/TiO$_2$, TiO$_2$/SnO$_2$, ZnO/SnO$_2$ [30]. The authors highlighted the mechanisms of bilayer photo-anodes for PEC water splitting. It was pointed out that bilayer structures provide proficient charge carrier transfer across the interface between the semiconductors which results in reduced charge recombination. Phuan et al. reviewed the prospects of hematite that is electrochemically synthesized [31]. The authors highlighted parameters that control pristine hematite morphology such as electrolyte precursor, electrode substrate, annealing treatment, and applied potential [31]. Esmaili et al. reviewed the importance of a nanostructure morphology on the performance of a PEC water-splitting cell [32]. The authors pointed out that the electronic structure and morphology of the semiconductor used are key performance parameters in PEC water splitting. Various morphology dimensions of 0-D, 1-D, 2-D, and 3-D were discussed in detail [32]. Saraswat et al. reviewed the synthesis schemes of photo-catalysts that result in better catalytic performance at PEC water splitting and the various corresponding challenges faced in the photo-catalyst architecture build-up [33]. The authors pointed out that, morphology can be controlled by preparation method, calcination temperature, and crystal geometry or structure, which is in agreement with the views of Phuan et al. [31, 33]. Iqbal and Siddique reviewed work on carbon-based photo-anodes used for PEC water splitting such as hematite/Graphene heterojunction nanowires, carbon and Fe$_2$O$_3$ quantum dots, and carbon nanotubes, among others [34]. Raza et al. recently analyzed research work on several 2-D layered photo-anodes and photocathodes [35]. The main focus was on how 2-D materials provide PEC application in energy conversion. Jun et al. recently reviewed the superiority properties exhibited by 2-D materials in comparison to their 0-D, 1-D, and 3-D counterparts [36]. The authors focused on how 2-D materials are synthesized and how they are used for PEC water splitting based on their roles as light harvesters, catalysts, interfacial transporting layers, and as passivation layers. The 2-D materials include; Graphitic carbon nitrides, layered double hydroxides, Mxenes, and transition metal dichalcogenides [35, 36]. Recently, Wan et al. reviewed the effect of electronic structures or compositions on the practical performance of hematite [21]. Li et al. reviewed heterojunctions and their advantages if employed as photo-anodes in PEC water splitting [37]. The different types of heterojunctions such as the type II and Z-scheme were introduced and their physical effects on the enhancement of carrier transfer in a material were discussed. Young and co-workers reviewed the strategies to facilitate charge transfer for enhanced oxygen evolution, reviewed articles on transitional and ternary metal oxides [38–40]. Figure 1 provides a summary of the work that has been published on hematite for PEC water splitting obtained from the Web of Science. Figure 1a shows research articles on hematite, Fig. 1b shows the review articles on hematite, Fig. 1c shows research articles on hematite hetero-structures and Fig. 1d shows the review articles on hematite hetero-structures. In general, the graphs depict an increasing trend for hematite as a potential PEC material. Despite the increasing trend, there are very few review articles that have been published focusing on hematite and its hetero-structures. In addition, most of the published review articles lack scientific rationale on how the measured properties are affected by the electronic properties such as electrical conductivity and charge carrier mobility of the hetero-structure/substrate. This review offers the latest developments and provides further insights into the different hematite hetero-structures in relation to their PEC performance. This review article is organized as follows: a brief PEC background, PEC performance parameters, types of PEC device configurations, and the physical and crystallographic properties of hematite. The review further discusses the performance of hematite and its hetero-structures on Fluorine-doped Tin Oxide (FTO), Sn-doped In$_2$O$_3$ (ITO), and other substrates.

2 Principle of operation photoelectrochemical water splitting device

The first PEC water-splitting device was created by Funjishima and Honda in 1972 and used TiO$_2$ (the rutile phase) and Pt as photo-anode and photocathode respectively to convert UV irradiation into hydrogen [5]. Figure 2 shows the PEC system with two reference energy levels, normal hydrogen energy (NHE) and vacuum level (Fig. 2a). PEC system before equilibrium in the dark (Fig. 2b), the PEC system at illumination (Fig. 2c), and the PEC system after illumination (Fig. 2d). When the semiconductor is immersed in the electrolyte, a solid–liquid interface is created between the semiconductor and the electrolyte. As a result, electron transfer takes place between the working electrode, the electrolyte, and the
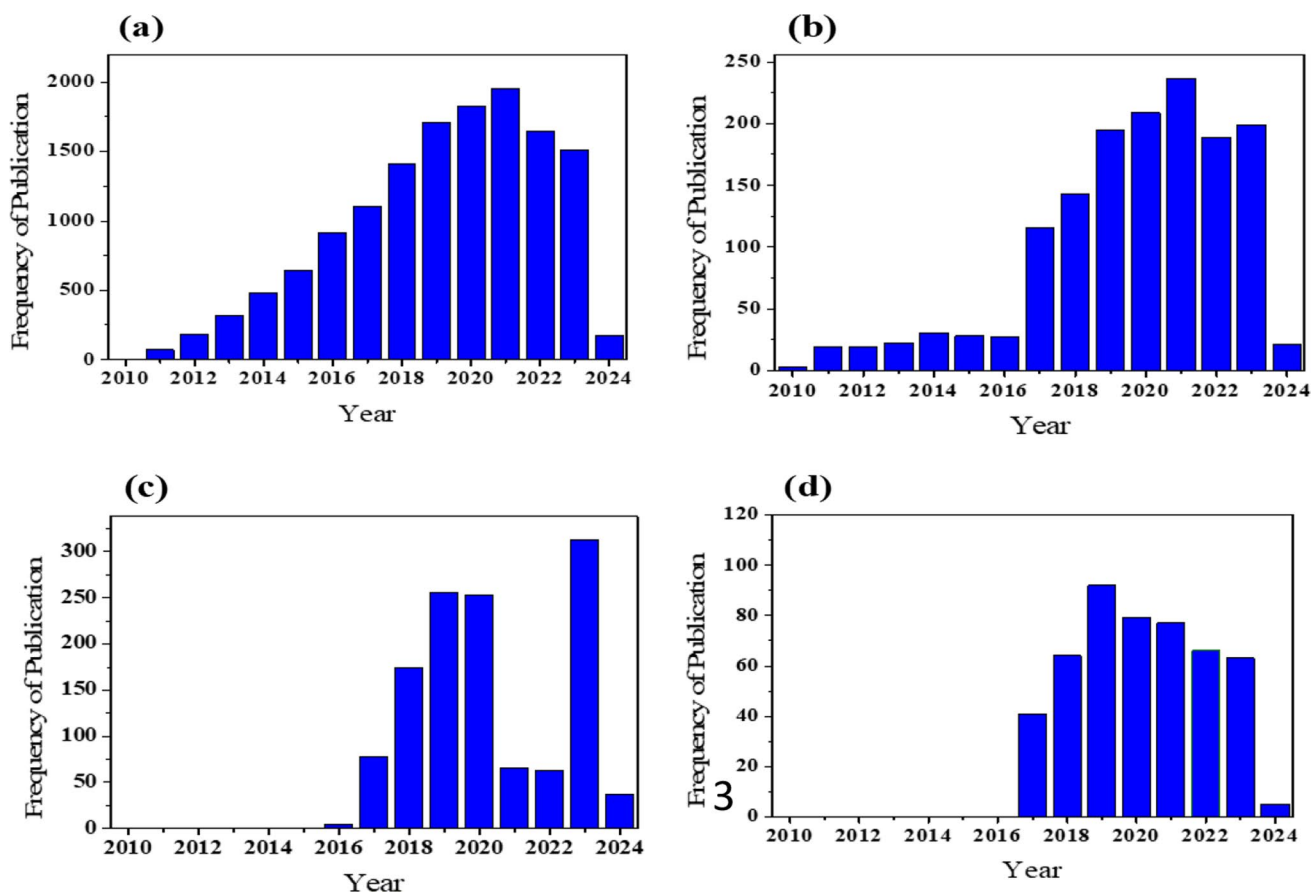
Fig. 1 A comparison of published work for PEC water splitting from 2010 to date; **a** research articles on hematite, **b** review articles on hematite, **c** research articles on hematite hetero-structures, and **d** review articles on hematite hetero-structures
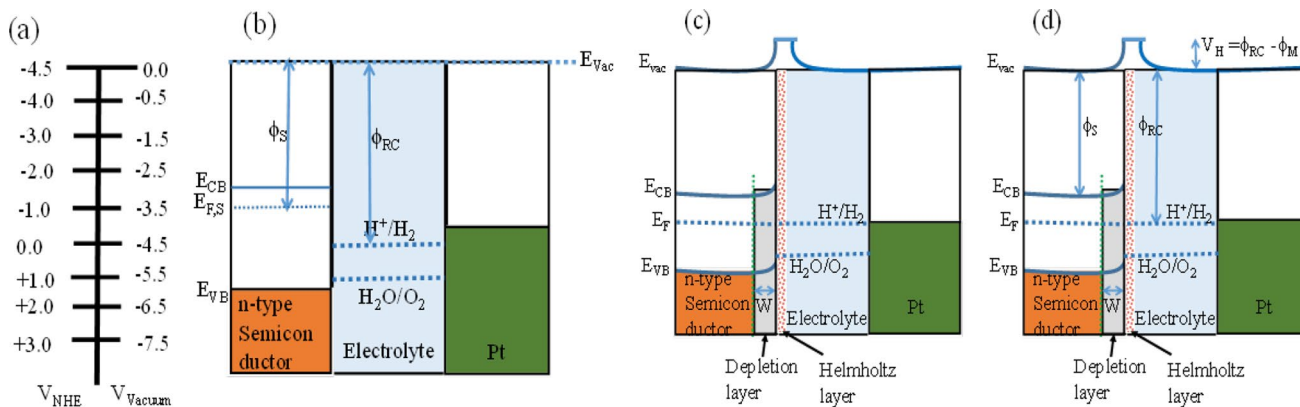

Fig. 2 **a** Electrochemical energy levels, **b** energy band diagram of a PEC system before equilibrium, **c** energy band diagram of PEC system at equilibrium in the dark condition and **d** energy band diagram of PEC system under illumination

counter electrode until the Fermi levels of the semiconductor, the counter electrode, and the electrolyte line up as shown in Fig. 2b [41–43]. Electrons will flow from the photo-anode (higher Fermi level) to the electrolyte and then to the counter electrode (lower Fermi level). After the Fermi levels have line-up, the semiconductor will have an excess of positive charge, arising from the immobile ionized impurity atoms, and the electrolyte will have an excess of negative charge. As a result of the movement of electrons, a depletion layer with width "W" is created in the semiconductor side and the

negative charge accumulates over a much narrower region called the Helmholtz layer between the electrode and the electrolyte as shown in Fig. 2 c. On illuminating the semiconductor with photon energy greater than the band gap of the semiconductor, electron–hole pairs will be generated. The electrons will be excited to conduction band, leaving the holes in the valence band. As shown in Fig. 2d, a quasi-Fermi level is established whose gradient results into the built-in electric field or the open-circuit voltage (V_{OC}). The electrons are transferred to the counter electrode to generate hydrogen. The holes will diffuse to the surface of the semiconductor to generate oxygen [3, 43]. For water splitting to take place, the semiconductor's valence band (V.B.) potential must be more positive than the E_{OER} redox of 1.23 V vs NHE to allow oxidation, whilst the conduction band (C.B.) must be more negative than the E_{HER} redox potential of 0 V vs. NHE to carry out water reduction. This is in addition to overpotentials. The overall reaction of water splitting is illustrated by Eq. 1, and the hydrogen evolution reaction (HER) and oxygen evolution reaction (OER) are illustrated by Eqs. 2 and 3 respectively.

Combined PEC reaction;

$$2H_2O + 4hv \rightarrow O_2 + 2H_2 \tag{1}$$

Reaction at the anode;

$$4H^+ + 4e^- \rightarrow 2H_2 \tag{2}$$

Reaction at the cathode;

$$2H_2O + 4(h^+) \rightarrow O_2 + 4H^+ \tag{3}$$

The overall reaction requires the Gibbs free energy, $\Delta_r G^o$ of 273.2 kJ/mol [44]. In this connection, photons whose energy is equal to or greater than the band gap energy of the semiconductor material will be exited [34, 44]. Theoretically, the band gap should be larger than 1.23 eV because the difference between HER and OER is 1.23 eV. Practically, an energy gap between 1.5–1.8 eV is necessary due to HER/OER over potentials. The PEC water splitting process takes three steps, viz; absorption of light, separation and transportation of photo-generated charge carriers, and surface reduction as indicated in Fig. 2b [34, 44, 45].

2.1 The most common PEC device configurations in literature for Hematite

2.1.1 Single semiconductor photoanode light absorber configuration

This configuration is similar what has been explained in Fig. 2. When an n-type semiconductor (whose work function is lower than the work function of the metal) and an electrolyte come into contact, electrons flow from the semiconductor toward the counter electrode via the external circuit well as holes are transferred into the electrolyte until equilibrium is reached. At this point, the semiconductor/electrolyte interface is depleted of electrons compared to the electrons in the semiconductor bulk hence a depletion layer forms and the bands bend upwards as shown in Fig. 3a [46]. The electrons take part in water reduction and the holes take part in the water oxidation [47, 48]. This kind of configuration creates barrier potential, that leads to improved charge separation [36, 47, 49, 50]. The electrons then take part in HER well as the holes take part in the OER. Hematite has been used as a single junction photo-anode for PEC applications.

2.1.2 Heterojunction semiconductor photoanode light absorber configuration

In this configuration, secondary semiconductors are developed onto the primary absorber to improve light absorption and charge separation [46]. In this configuration, the top layer will absorb high-energy photons but allow low-energy photons to go pass through as illustrated in Fig. 3b [51]. The low-energy photons will be absorbed by the subsequent layer hence improving photo-absorption. For this configuration to form, band gap variation and lattice matching are key [52]. Hetero-structuring provides properties that complement each semiconductor such as increased spectral range, enhanced interfacial charge carrier mobility, strong interfacial built in electric field and thus effective interfacial charge carrier transfer[53–56].
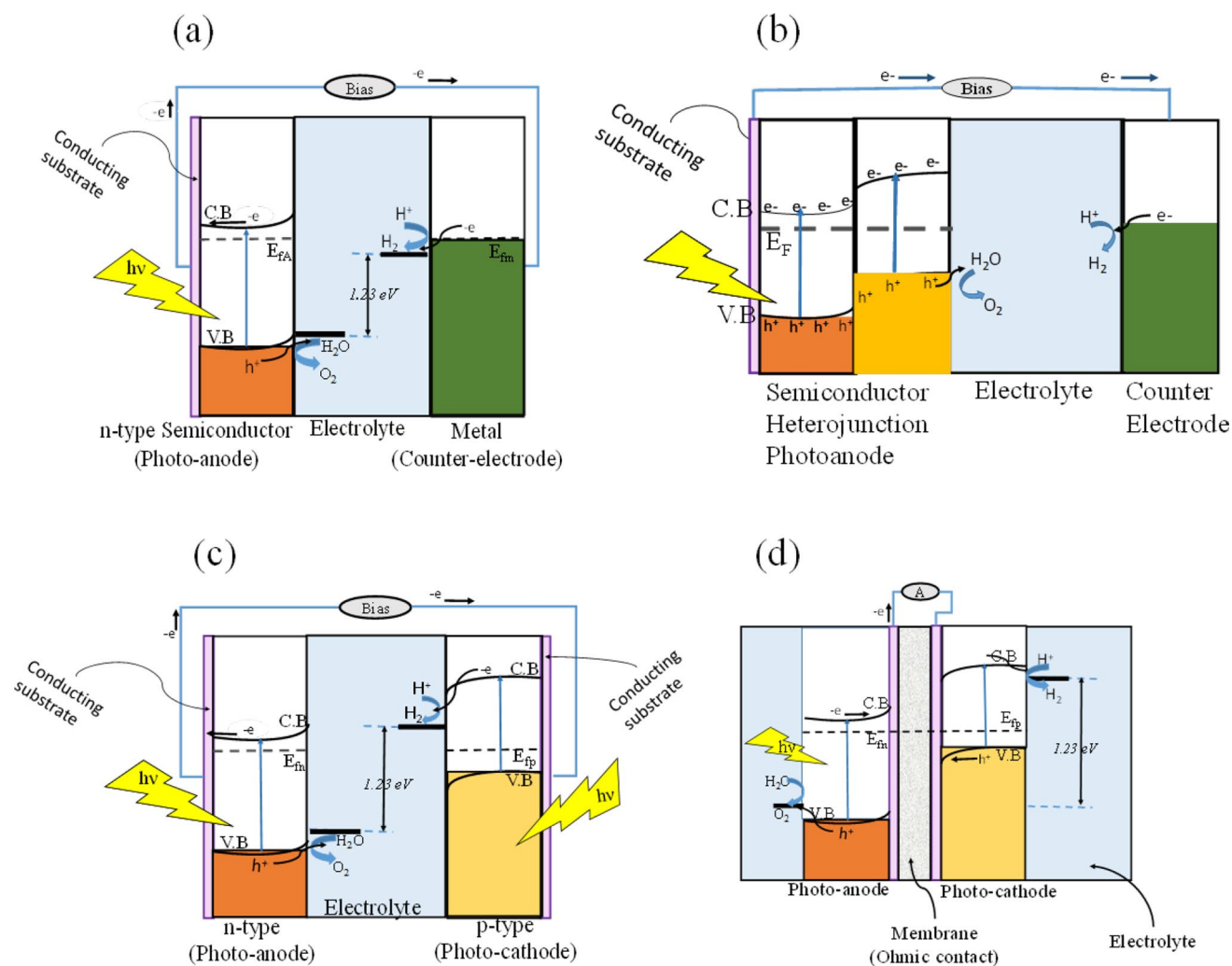
Fig. 3 Schematic band diagrams illustrating **a** single n-type semiconductor photo-anode/metal counter-electrode, **b** semiconductor heterostructure photo-anode/metal counter electrode, **c** with bias, and **d** tandem PEC cell configuration without

2.1.3 Series connected photoanode and photocathode (tandem)

In this configuration, two light absorbers are utilized as a Photoanode for water oxidation and a photocathode for water reduction. This configuration is subdivided into wired (operates under bias) and wireless configurations (operates without bias). One conductive metal wire can be used for the wired configuration and a transparent conductive substrate can be used as an electron–hole recombination layer for the wireless configuration. The separation membrane separates O_2 from H_2 [57]. Tandem cell configurations without bias minimize on the challenges of overpotential and Ohmic losses faced by single light absorber PEC devices [58]. The tandem cell in this configuration must have a photo-voltage at the photo-anode and photo-cathode that exceeds HER and OER potentials for overall water splitting (> 1.23 V) [47, 59]. Figure 3c shows an n-type photo-anode with a p-type photo-cathode connected by an external cicuit when operating with bias. On illuminating the photo-anode with photon energy greater than its band gap enegy, electron–hole pairs are photogenerated and separated, the electrons flow to the C.B. from the V.B. and via the external circuit to the photo-anode's C.B. well as the holes drift to the photo-anode surface [58]. Figure 3d indicates the operation of a Tandem PEC cell without bias where on irradiation, a space charge field is set up enabling separation of the photogenerated electron–hole pairs where the p-type photo-cathode electrons drift to the semiconductor/electrolyte interface to take part in the reduction process well as the holes in the n-type photo-anode drift to the semiconductor/electrolyte interface to take part in the oxidation process [25, 60].

3 Properties of hematite

3.1 Crystallography

Hematite has rhombohedral lattice structure with a space group of $R\bar{3}c$. The lattice parameters at room temperature are a = b = 0.5034 nm, c = 1.375 nm, and γ = 120° [4, 5, 21, 37, 61–63]. The XRD peaks are indexed at (110), (101), (200), and (211) at 2θ values of 26.5°, 33.5°, 37.5°, and 51.5° respectively [64–67]. Its space group is P42/mnm with lattice parameters, *a* and *c* of about 4.74 Å and 3.19 Å respectively [65, 68]. Hematite when deposited on an FTO substrate gives peaks at 2θ ~ 24.1°, 33.1°, 35.6°, 40.9°, 49.4°, 54.0°, and 64.0° corresponding to (012), (104), (110), (113), (024), (116), and (300) planes respectively [69]. Of these, the peaks at (104) and (110) are predominant well as other FTO peaks are suppressed—an indication that the film has water in it and so the Fe^{3+} ions in the hematite film interact with the hydroxyl groups [66, 70]. FTO peaks may not be observed on the XRD chart if the film grown on them is thick, though when observed for such films, it is an indication that all water has been removed from the film and the extent of water removal is depicted in the intensity of the observed peaks [70, 71]. Hematite on FTO has a lattice parameter, *a* of 5.04 Å, and *c* as 13.74 Å (Fig. 4).

3.2 Optical properties

Hematite has a band gap that ranges between 1.9–2.2 eV and absorbs both partial visible light and ultraviolet light [7, 9, 21, 60, 73]. The photon penetration depth ranges between 100–120 nm at a wavelength of about 550 nm [74, 75]. This results in the generation of charge carriers relatively far from the hematite/electrolyte interface, hence not contributing significantly towards the water oxidation reaction. Also, at a wavelength of about 550 nm, hematite experiences low absorptivity hence the preference of synthesis of thick hematite films so as to absorb a sufficient amount of the sunlight for optimum PEC performance [9].

3.3 Electrical properties

Hematite is an n-type semiconductor with an electrical conductivity approximated at about $10^{-4}–10^{-6}$ Ω^{-1} cm^{-1}, charge carrier mobility of approximately 10^{-2} cm^2V^{-1} s^{-1}, and a carrier decay rate of < 1 ps [3, 5, 9, 31, 75–77].

4 Surface morphology of hematite on different substrate

1 D Nano-porous films, Nano flakes, Nano-tubes, or Nano-wires of hematite have been formed on an Fe foil, 3 D hematite like-Nano-flower- films have been formed on an FTO glass substrate as shown in Fig. 5a–d [10, 19, 31, 78]. 3-D structure arrays like Nano-spikes, Nano-wells, Nano-cones, and Nano-pillars enlarge the materials' surface area and hence enhance light absorption [79, 80].

Fig. 4 A schematic diagram showing the crystal structure of hematite where the large circles indicate Fe ions and the small circles indicate the O ions (Reproduced with permission from reference [72], copyright 2014, AIP publishing)
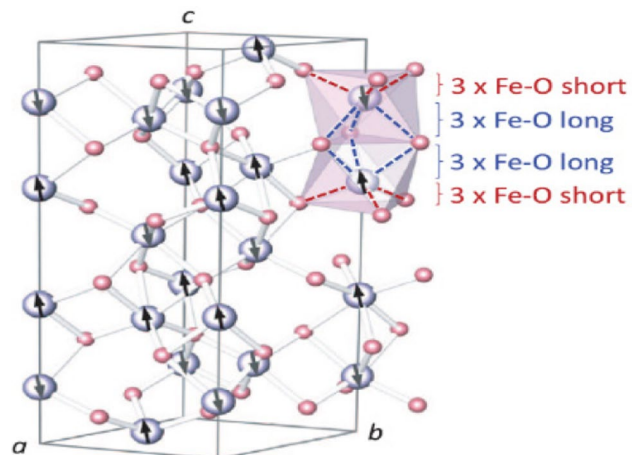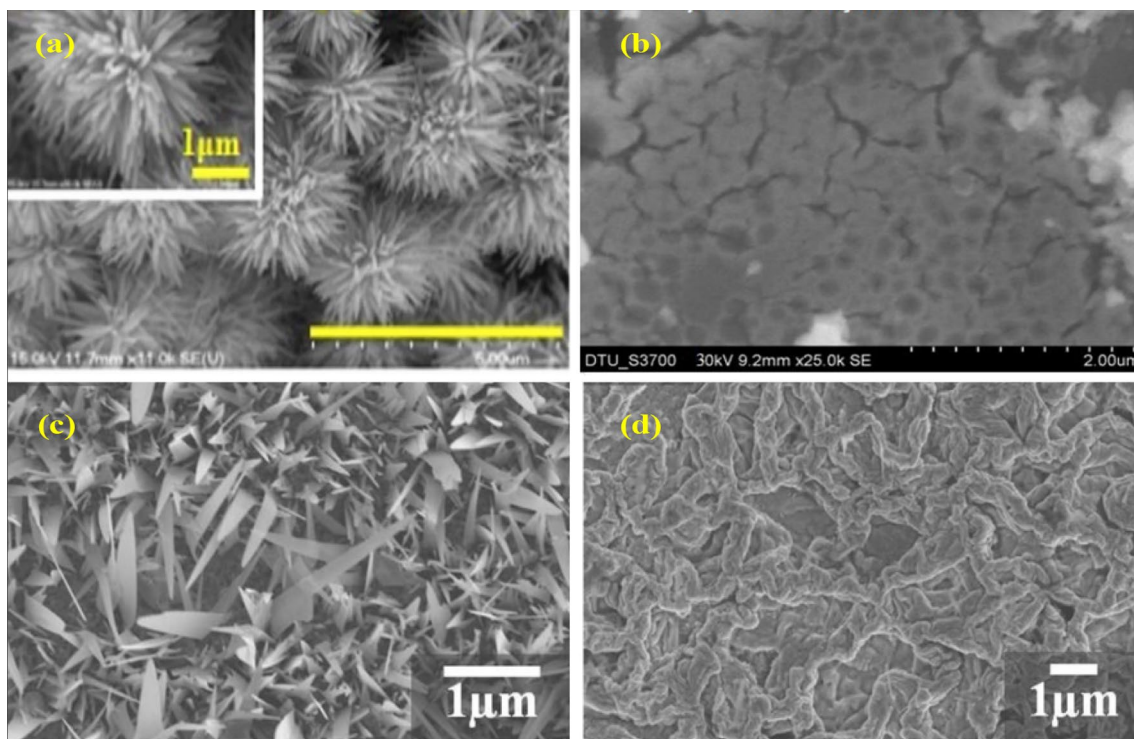
Fig. 5 SEM images showing the morphology of hematite on different substrates: **a** a 3 D flower-like film of pristine hematite on FTO glass substrate (Reproduced with permission [19] copyright 2016, Elsevier), **b** a porous morphology of Ti-Fe$_2$O$_3$/Cu$_2$O heterojunction on an ITO glass substrate **b** (Reproduced with permission [78] copyright 2014, Elsevier B.V), **c** nano-flakes of pristine α-Fe$_2$O$_3$ sintered at 400 °C on an Fe foil substrate, **d** a coral-like morphology is obtained when sintered at temperatures above 600 °C (Reproduced with permission [10] copyright 2020, Elsevier)

5 PEC performance of hematite on different substrates

Different substrates have different physical properties. Fluorine-doped tin oxide (FTO) and tin (Sn)-doped In$_2$O$_3$ (ITO) are the commonly used TCOs [81].

5.1 Physical properties of FTO glass substrate

FTO is an n-type semiconductor with a band gap of 3.8 eV [82] and a work function of 4.8–5.0 eV vs vacuum (0.3–0.5 eV vs R.H.E) [28, 30].The optical transmittance ranges between 60–90%, chemically and thermally stable, and has a high resistance to physical etching [67, 83]. FTO has a resistivity of about 3.5×10^{-4} Ωm, charge mobility of about 25 cm^{2}V^{-1} s^{-1}, and a carrier density of about 4.5–6×10^{20} cm^{-3} for thickness greater than 500 nm [84]. If doped with 2.5% F concentration, the electrical resistivity is about 6×10^{-4} Ωcm and a carrier density is of about 1.84×10^{20} cm^{-3} [65].

5.2 PEC performance of hematite on FTO substrates

In this section, we examine the performance of various morphologies of pristine and heterojunction hematite on FTO substrates.

5.2.1 FTO/Hematite/electrolyte/Pt configuration

Farhoosh et al. synthesized a Fe$_2$O$_3$/FTO photo-anode of nano-rod morphology via hydrothermal synthesis obtaining a 3.34×10^{19} cm^{-3} donor density, a 0.5 V flat band potential and a less than 1% IPCE value with a 0.003% ABPE value

taken at 1.1 V vs RHE [1]. Zhang et al. fabricated a bead array α-Fe$_2$O$_3$/FTO photo-anode and only managed to obtain a 0.46 mAcm^{-2} photocurrent density, a 0.461 V flat band potential with an IPCE value of 7.2% [85]. This shows very low performance exhibited by hematite if used in a single photo-absorber PEC device configuration. Table 1 shows a number of study findings for FTO/Hematite/Electrolyte/Pt PEC device set ups.

5.2.2 FTO/hematite heterojunction/electrolyte/Pt configuration

The formation of heterojunctions provides improved length of hole diffusion and lead to reduced charge recombination in the photo-electrode. This results in improved donor density and photocurrent density hence better overall conductivity of the photo-electrode.

The electrical conductivity of a semiconductor is related to carrier concentration (n), charge (e) and carrier mobility (μ) by

$$\sigma = ne\mu \tag{4}$$

and thus the increase in donor density increases the electrical conductivity. Likewise, photocurrent density (J) is related to electrical conductivity and electric field ($\vec{E}$) by

$$J = \sigma\vec{E} \tag{5}$$

This equation emphasizes that an increase in electrical conductivity increases the current density and thus the observed effects [98]

Where multiple junctions have been studied, it is noted that these enhance charge carrier photo-generation at the depletion layer leading to increased PEC performance of the heterojunction hematite photo-electrode. For instance, Farhoosh et al. synthesized Ti–Fe$_2$O$_3$/Fe$_2$TiO$_5$/FeOOH/FTO photo-anode through hydrothermal synthesis realizing a photocurrent density of ~ 1.63 macm^{-2} [1]. Fe$_2$TiO$_5$ and α-Fe$_2$O$_3$ have similar band gaps (2.1 eV for both) and were arranged with hematite as the under-layer onto an FTO substrate to form an n–n junction. As shown in the schematics of Fig. 6a(i), on illumination through the FTO side, electrons drift across the α-Fe$_2$O$_3$/FTO junction towards the Pt counter electrode via the external circuit while the holes drift across the Fe$_2$TiO$_5$/α-Fe$_2$O$_3$ junction to take part in the water oxidation process at the photo-anode/electrolyte interface. The Fe$_2$TiO$_5$ layer improved on the electrical conductivity by acting as a charge separator between the Ti-Fe$_2$O$_3$ and FeOOH layers.

For photo-generation of charge carriers to be effective, the C.B. and V.B. edges must suitably align. Therefore, band bending is inevitable. Here, the different Fermi levels of the semiconductors align through adjustment of the energy bands once the semiconductors come into contact. This results in a single Fermi-level for the hetero-structure as shown in Fig. 6(i) for each case. In this case, the positioning of the C.B. and V.B. is key. The electrons drift from a higher C.B. to a lower C.B. well as holes drift from a lower V.B. to a higher one. The drift through more junctions helps in improving the length the holes drift through to hit the photo-anode/electrolyte interface to take part in water oxidation. Thus better photocurrent density in the heterojunction photo-anode is obtained as indicated in Fig. 6(ii) for each case. With these band edge positions in mind, for instance, Fig. 6 (i), (b) with p-CaFe$_2$O$_4$/n-Fe$_2$O$_3$ at a band gap of 1.9 eV and 2.1 eV respectively, (d) with FeNbO$_4$ at 1.91 eV and Fe$_2$O$_3$ at 2.1 eV, and (e) with SnO$_2$ at 3.8 eV and Fe$_2$O$_3$ at 2.1 eV, it is noted that the built-up hetero-structures used the semiconductor with a higher band gap as the under-layer on FTO substrate, well as (g), (h), and (i) indicate the reverse. With p-CaFe$_2$O$_4$/n-Fe$_2$O$_3$, a p–n junction photo-anode was formed where on illumination, holes in the n-Fe$_2$O$_3$ were reported to be excited into the V.B. of p-CaFe$_2$O$_4$ well as electrons were transferred from the C.B. of p-CaFe$_2$O$_4$ to the C.B. of n-Fe$_2$O$_3$ to reach the back contact as shown in Fig. 6b(i) [87]. The presence of the heterojunction in p-CaFe$_2$O$_4$/n-Fe$_2$O$_3$/FTO photo-anode allows for efficient electron–hole pair separation at the heterojunction. With the presence of a Co-Pi, hole capturing at the photo-anode/electrolyte interface resulting in better charge separation hence reducing their accumulation which usually results in recombination experienced in the n-Fe$_2$O$_3$/FTO photo-anode. In Fig. 6f(ii), with p-LaFeO$_3$/n-Fe$_2$O$_3$/FTO p–n junction photo-anode, effective charge separation at the p–n junction was realized giving a photocurrent density of 0.58 mAcm^{-2} which was as well not impressive [2]. Here, during band edge matching (band bending at the interface), the V.B. of LaFeO$_3$ is more negative than that for Fe$_2$O$_3$ which results in reduced oxygen evolution driving force at the junction. This in addition gives slow reaction kinetics at the interface hence low performance even with the heterojunction. Applying a CoO$_x$ layer (catalyst) on the p-LaFeO$_3$ surface to form CoO$_x$/p-LaFeO$_3$/n-Fe$_2$O$_3$/FTO results in a better photocurrent density value recorded at 1.12 mAcm^{-2}. From Fig. 6g(i), in the heterojunction

Table 1 Work done on pristine hematite developed on FTO glass substrate

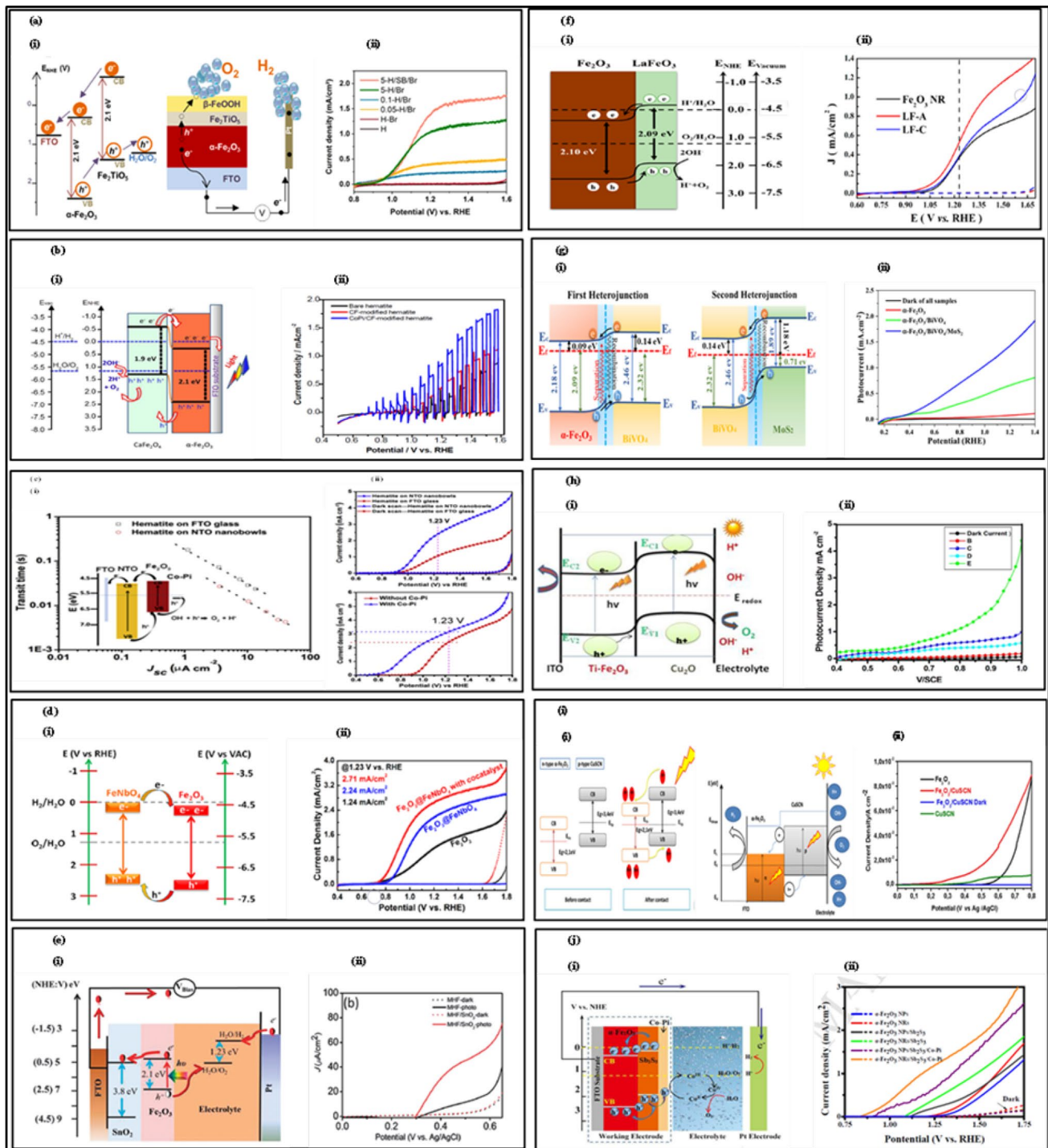| Device architecture	Surface morphology	Photocurrent density, J (mAcm^{-2}) taken under 1 sun at 1.23 V vs RHE	Flat band potential, V_{fb} (V) vs Ag/AgCl	Donor density, N_d ($\times 10^{19}$) (cm^{-3})	Performance efficiency (%) (taken in the range of 350–450 nm irradiation with an applied potential window from 0.50–1.80 V)	References
α-Fe$_2$O$_3$/FTO	Bead array	0.46	0.461		7.2 (IPCE)	[85]
α-Fe$_2$O$_3$/FTO	Crystalline planes	0.0044	0.26			[86]
Fe$_2$O$_3$/FTO	Nano-rods	0.84		0.81	27.1 (IPCE)	[8]
n-Fe$_2$O$_3$/FTO	Nano-rods	0.20		44.0		[87]
NP-H/FTO	Nonporous nanoparticles	0.012	−0.524	0.000668		[7]
MHF/FTO	Mesoporous hematite thin films	0.012	−0.445	0.000425	0.011 (IPCE)	[7]
n-Fe$_2$O$_3$/FTO	Nano-rods	0.37	0.42	119	10.11 (IPCE)	[2]
Ti:Fe$_2$O$_3$/FTO	Nano-particles	1.02			10.8 (IPCE)	[18]
α-Fe$_2$O$_3$/FTO	Irregular rice shaped Nano-rods	0.10			1.8 (IPCE) 0.015 (ABPE)	[88]
Fe$_2$O$_3$/FTO	Thin films	0.16	−0.49		0.18 (IPCE) 0.06 (ABPE)	[78]
Ti:Fe$_2$O$_3$/FTO	Thin films	0.80	−0.70		2.10 (ABPE) 0.35 (IPCE)	[78]
Fe$_2$O$_3$/FTO	Nano-rods	0.26	0.49	2.23	4.40 (IPCE)	[89]
α-Fe$_2$O$_3$/FTO	Nano-rods	0.14				[90]
α-Fe$_2$O$_3$/FTO	Nano-rods	0.38	0.77	32.4		[91]
α-Fe$_2$O$_3$/FTO	Nano-rods	0.72			0.050 (ABPE)	[92]
α-Fe$_2$O$_3$/FTO	Nano-structured grains	0.005		160		[69]
α-Fe$_2$O$_3$/FTO	Nano-structured grains	0.4				[93]
α-Fe$_2$O$_3$/FTO	Lava-shaped and spherical Nano-particles	0.027	0.30	4.5		[94]
α-Fe$_2$O$_3$/FTO	Smooth Nano-particles	0.57		0.030	20 (IPCE)	[95]
Fe$_2$O$_3$/FTO	Nano-rods	0.027				[96]
Ti:Fe$_2$O$_3$/FTO	Fine Nano-rods	0.800			6.0 (IPCE) 0.07 (ABPE)	[96]
Fe$_2$O$_3$/FTO	Nano-wires	0.205		0.46	2.1 (IPCE)	[97]

Fig. 6 Images of schematic diagrams showing hetero-structure build-ups and their corresponding photocurrent density comparisons with pristine hematite photo-anode performances on FTO glass substrates in photo-absorber photoanode/metal counter electrode configuration, (Adopted with permission **a** [1] copyright 2021, Elsevier B.V, **b** [87] copyright 2015, ACS Publications, **c** [18] copyright 2017, Elsevier, **d** [8] copyright 2019, ACS Publications, **e** [7] copyright 2013, RSC Publishing, **f** [2] copyright 2017, ACS Publications, **g** [88] copyright 2021, Elsevier, **h** [78] copyright 2014, Elsevier B.V, **i** [69] copyright 2017, IOP Publishing, and **j** [99] copyright 2018, Elsevier B.V

photo-anode (MoS_2/$BiVO_4$/α-Fe_2O_3/FTO) electrons move from the C.B. of MoS_2 to that of $BiVO_4$ then to the C.B. of α-Fe_2O_3 through the FTO substrate then via the external circuit to the counter-electrode, while the electrostatic field drives the holes from the V.B. of α-Fe_2O_3 to that of $BiVO_4$ and then to that of MoS_2 this takes part in the oxidation reaction [88].

Tremendously improved results for hematite PEC performance are realized once more than one strategy is applied in the formation of a hematite photo-anode. For instance, Sharma et al. strategized with doping Fe_2O_3 with Ti and then hetero-structuring it with Cu_2O and gained a big improvement in the performance of hematite at PEC water splitting [78]. An IPCE value of 6.5% for the doped hematite hetero-structure (Cu_2O/Ti-Fe_2O_3/FTO) with respect to 0.18% for pristine hematite photo-anode were recorded. Also a photo-anode of $FeNbO_4$/Fe_2O_3/FTO, Sn and Nb doping into Fe_2O_3 at the Fe_2O_3/FTO and $FeNbO_4$/Fe_2O_3 interfaces respectively developed by Zhang et al. results in better charge carrier density in the doped heterojunction photo-anode relative to the pristine hematite photo-anode that is at 1.77×10^{19} cm^{-3} and 0.81×10^{19} cm^{-3} respectively [8].

In another recent study, Zhang et al. fabricated a Voα-Fe_2O_3/AuNSs/FTO heterojunction photo-anode realizing a better photocurrent density of 1.46 mAcm^{-2} in relation to the 0.46 mAcm^{-2} from the α-Fe_2O_3/FTO photo-anode [85]. This improvement was attributed to improved bulk conductivity and exhibition of surface electrocatalytic ability by the heterojunction photo-anode. Here, charge recombination is suppressed due to the strong AuNSs and α-Fe_2O_3 interface contact which improves on band bending in addition to the oxygen vacancy (Vo) presensence reducing on the activation energy provided by increased holes. Table 2 shows the various hematite heterojunction photo-absorber PEC performances.

5.2.3 FTO/hematite tandem configuration

Vilanova et al. designed a compact optimized open light PEC cell (CoolPEC cell) of a tandem configuration in which hematite was used as a working-electrode, an anion as the exchange membrane, and platinized-Ti mesh as a counter-electrode [100]. Using cyclic holders, the platinized-Ti mesh was held firmly to the membrane and the hematite photo-anode to reduce the Ohmic losses at the contact points resulting in a 0.45 mAcm^{-2} photocurrent density. The test was done using a 2-electrode configuration under 1000 Wm^{-2} solar simulation. According to Landman et al., this single-cell configuration is efficient for small-scale hydrogen production rather than large-scale due to the high maintenance and membrane costs involved [101]. Therefore, the researchers recommend setting up separate cell configurations for oxygen and hydrogen production known as the PEC-PV configuration where a membrane is not necessary since the two gases will be produced in different cells. Gurudayal et al. examined the performance of pristine hematite in tandem connection with a mesoporous perovskite solar cell as shown in the schematic in Fig. 7a recording a photocurrent density of 1.33 mAcm^{-2} shown in Fig. 7b with a fill factor of the perovskite solar cell at 0.62, and a STH efficiency of 1.5 [102]. in another study, Gurudayal et al. modified hematite photoanodes with SnO_x via hydrothermal synthesis followed with the atomic layer deposition technique [103]. These modified Sn-doped Fe_2O_3 Nws photoanodes were set-up in tandem with a $CH_3NH_3PbI_3$ perovskite solar cell realizing a 4.5 mAcm^{-2} photocurrent density and a 3.4% STH efficiency. Table 3 shows studies on hematite in a Tandem PEC cell set-up.

5.3 Physical properties of ITO glass substrate

An ITO glass substrate is an n-type semiconductor with a relatively wide band gap energy approximated at 3.5–4.3 eV [82, 104]. ITO glass substrates bear good optical properties, that is an optical transmittance of about 80–90% [67]. An ITO glass substrate exhibits a cubic structure of the la-3 space group with lattice parameter a ~ 10.130 Å [64, 65, 105, 106] and with a crystalline grain morphology [65, 107]. For a thickness above 100 nm at Sn/In concentrations of 2.4%/4.8% respectively, an ITO glass substrate has an electrical resistivity of about $3–4 \times 10^{-4}$ Ω, a carrier density of about $4–10 \times 10^{20}$ cm^{-3} and a mobility of about 35 cm^{2}V^{-1} s^{-1} [84]. With a Sn concentration at 6%, the electrical resistivity is about 8×10^{-4} Ω, and the carrier density is about 3.67×10^{20} cm^{-3}. This increased resistivity is attributed to high free electron concentrations due to substitutional Sn and oxygen vacancies in addition to ITO having a cubic structure [65]. The mobility of ITO can be reduced to about 20 cm^{2}V^{-1} s^{-1} at temperatures above 400 °C.

5.4 PEC performance of hematite on ITO

Riha et al. and Kaouk et al. agree that annealing at such high temperatures results in reduced conductivity of hematite on ITO substrates since such temperatures result in increased resistance of the hematite/ITO photo-anode [108, 109]. Here, more Sn atoms in the crystal are localized on the interstitial lattice sites, or a radius mismatch is observed which results in distortion of the crystal structure. Also, such temperatures reduce the oxide layers into metallic indium layers [84]. This results in localized Sn atoms acting as ionized scattering centers.

Table 2 Work done on hematite heterojunction photoabsorber for PEC water splitting

Device architecture	Surface morphology	Photocurrent density, J (mAcm^{-2}) taken under 1 sun at 1.23 V vs RHE	Flat band potential, V_{fb} (V) vs Ag/AgCl	Donor density, N_d (×10^{19}) (cm^{-3})	Performance efficiency (%) (taken in the range of 350–450 nm irradiation with an applied potential window from 0.50–1.80 V)	References
Vo α-Fe$_2$O$_3$/ AuNSs/FTO	Defected bead array	1.46	−0.397		25 (IPCE)	[85]
FeNbO$_4$/Fe$_2$O$_3$/FTO	Nano-rods	2.24		1.77	45.8 (IPCE)	[8]
MHF/SnO$_2$/FTO	Worm-like pore structure	0.045	−0.406	0.000425	0.046 (IPCE)	[7]
CuO/Fe$_2$O$_3$/FTO	Nano-rods with increased diameter	0.70	0.34	7.79	11.41 (IPCE)	[89]
α-Fe$_2$O$_3$/γ-Fe$_2$O$_3$/FTO	Ordered Nano-rods	0.74				[90]
α-Fe$_2$O$_3$/γ-Fe$_2$O$_3$/FTO	Disordered Nano-rods	0.33				[90]
α-Fe$_2$O$_3$/sIr/FTO	Amorphous layer (Ir dots) on hematite surface	0.0575	0.36			[86]
CdO/α-Fe$_2$O$_3$/FTO	Nano-poles	1.20	0.56	280	0.10 (ABPE)	[91]
β-FeOOH/α-Fe$_2$O$_3$/FTO (FTO/5–H/Br)	Branched Nano-rods	1.23	0.88	18.69	15.9 (IPCE)	[1]
p-LaFeO$_3$/n-Fe$_2$O$_3$/FTO	Weak nano-rod clusters	0.58	0.32	538	15.47 (IPCE)	[2]
BiVO$_4$/α-Fe$_2$O$_3$/FTO	Porous and dense Nano-particle layers on Nano-rods	0.70			8 (IPCE) 0.071 (ABPE)	[88]
CuO/α-Fe$_2$O$_3$/FTO	Spherical Nano-structure	0.53	0.64	17.5		[94]
rGO/α-Fe$_2$O$_3$/FTO	3-D Urchin-like structure agglomerated from Nano-rods with rod-like crystallites radiating from the center	1.06			0.102 (ABPE)	[92]
Fe$_2$O$_3$/ITO/FTO	Nano-wires	1.050		2.75	14.8 (IPCE)	[97]
Cu$_2$O/Fe$_2$O$_3$/FTO	Porous thin films	0.50	-0.65		1.00 (IPCE) 0.21 (ABPE)	[78]
Cu$_2$O/Ti:Fe$_2$O$_3$/FTO	Granular porous thin films	2.60	−0.87		6.50 (IPCE) 1.21 (ABPE)	[78]
α-Fe$_2$O$_3$/ZnO/FTO	Nano-rods	2.4				[93]
Sb$_2$S$_3$/α-Fe$_2$O$_3$-NPs/FTO	Smooth Nano-particles	0.19			~ 3 (IPCE)	[99]
Sb$_2$S$_3$/α-Fe$_2$O$_3$-NRs/FTO	Smooth Nano-rods	0.36	0.04		~6 (IPCE)	[99]
p-CuSCN/α-Fe$_2$O$_3$/FTO	Mixture of leafy intrinsic trigonal pyramid shapes with bigger grains	0.015		280		[69]
CuAl-LDH/Ti:Fe$_2$O$_3$/FTO	Nano-sheets on top of Nano-rods	0.920			10.0 (IPCE) 0.08 (ABPE)	[96]
Cu$_2$O/Ti:Fe$_2$O$_3$/FTO	Particles on Nano-sheets and Nano-rods	1.350			32.7 (IPCE) 0.11 (ABPE)	[96]

Table 2 (continued)

| Device architecture	Surface morphology	Photocurrent density, J (mAcm^{-2}) taken under 1 sun at 1.23 V vs RHE	Flat band potential, V_{fb} (V) vs Ag/AgCl	Donor density, N_d ($\times 10^{19}$) (cm^{-3})	Performance efficiency (%) (taken in the range of 350–450 nm irradiation with an applied potential window from 0.50–1.80 V)	References
SO-TiB$_2$/α-Fe$_2$O$_3$/FTO	Amorphous rough agglomerated Nano-particles	2.00		0.056	33 (IPCE)	[95]
β-FeOOH/FeTiO$_2$/α-Fe$_2$O$_3$/FTO (FTO/5-H/SB/Br)	Branched Nano-rods	1.63	0.88	52.23	0.11 (ABPE) 20.0 (IPCE)	[1]
p-CaFe$_2$O$_4$/n-Fe$_2$O$_3$/FTO	Nano-rods	0.53		86.0		[87]
CoO$_x$/p-LaFeO$_3$/n-Fe$_2$O$_3$/FTO	Uniform thin films covering nano-rod surface	1.12	0.31	3200	25.13 (IPCE)	[2]
MoS$_2$/BiVO$_4$/α-Fe$_2$O$_3$/FTO	Nano-sheet layers on longer Nano-rods	1.67	0.15	43.6	22 (IPCE) 0.28 (ABPE)	[88]
Co-Pi/Sb$_2$S$_3$/α-Fe$_2$O$_3$-NPs/FTO	Rough Nano-particles	0.60			~9 (IPCE)	[99]
Co-Pi/Sb$_2$S$_3$/α-Fe$_2$O$_3$-NRs/FTO	Rough Nano-rods	1.14	0.37		~18 (IPCE)	[99]
Fe$_2$TiO$_5$/Fe$_2$O$_3$/ITO/FTO	More straight Nano-wires	1.560		5.80	18.6 (IPCE)	[97]
FeNiOOH/Fe$_2$TiO$_5$/Fe$_2$O$_3$/ITO/FTO	Ultra-thin Nano-wires	2.200		7.00	28.7 (IPCE)	[97]
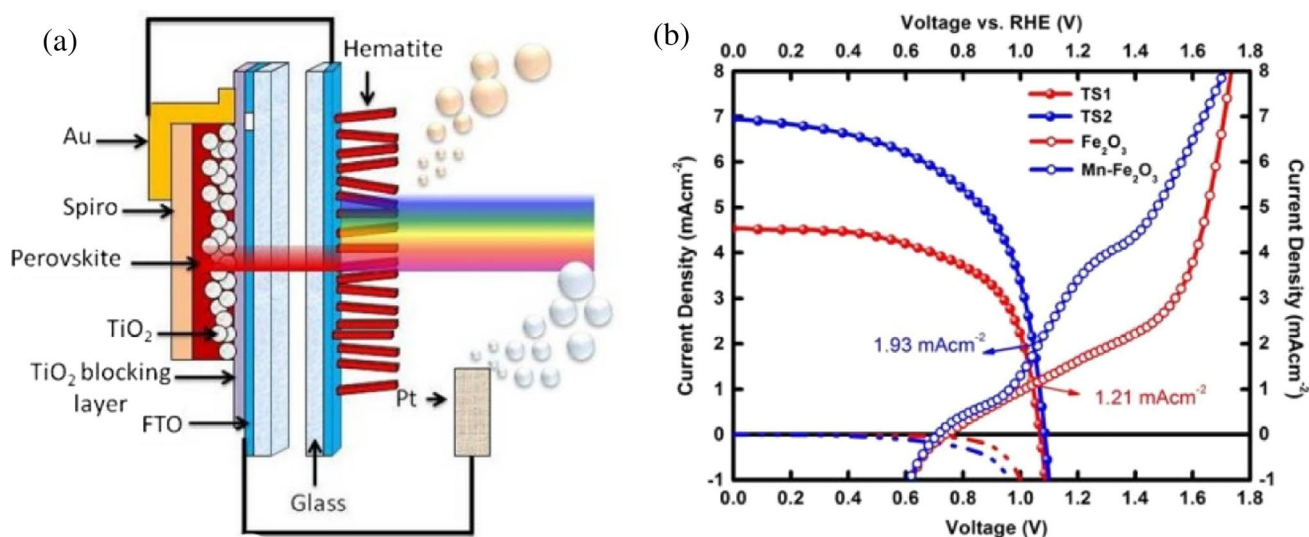
Fig. 7 **a** Image of a schematic showing a PEC-PV tandem cell set-up, and **b** corresponding performance at PEC water splitting (Adopted with permission [102] copy right 2015, NANO letters)

5.4.1 ITO/hematite/electrolyte/Pt configuration

According to Zandi and Haman, for efficient water oxidation, the photo-anode used should be of an n-type semiconductor since this provides efficient band bending for charge carrier separation [110]. In addition, He et al. suggest that homo-junctions can be formed to improve photon absorption [111]. In this regard, hematite/ITO build-ups produce a photo-anode of the n/n-type homo-junction since both hematite and the ITO substrate are small band gap and wide band gap n-type semiconductors respectively. The expectation here is that when hematite is grown on ITO, a balance of electrons and holes will take place at the interface hence a space charge zone will be created and an electric field will flow [111]. For instance, Yu et al. fabricated hematite homo-junctions with an ITO substrate by oxygen vacancy control and concluded that hematite bilayer films increased carrier concentrations in hematite resulting in modulation of the Fermi-level of hematite leading to the formation of the n–n hematite/ITO homo-junction [112].

Band gap energy is one of the fundamental materials' properties that determines the portion of solar spectrum absorbed by a semiconductor photo-absorber hence controlling its photo conversion efficiency [113]. The grain size for hematite nanoparticles is about 29 nm from HRSEM micrographs with a microstrain $\sim 0.3492 \times 10^{-3}$ from XRD peaks well as its band gap is increased to about 2.41 eV (outside the theoretical band gap range for hematite of 1.9–2.1 eV) when deposited on an ITO substrate by spin coating for 6 min in a study conducted by Kumar and Yadav—an indication of the presence of the Fe^{3+} ions in a low spin state [70]. On illumination, the absorbed photons excite electronic transitions though some do not lead to the generation of electron–hole pairs for instance if the d-d ligand transition is excited [113]. With this good optical property of hematite, Wang et al. also performed a theoretical optical simulation assuming an air mass of 1.5 solar spectra with a 20 nm film thickness (which is almost the hole diffusion length in hematite) and managed to derive the theoretically expected maximum photocurrent density of 12.5 $mAcm^{-2}$ for hematite grown on an ITO Nano-cone substrate [114].

Landolo et al. also carried out a study of α-Fe_2O_3 deposited on ITO and FTO by physical vapor deposition with heat treatment at 350 °C for a period ranging from 0 to 24 h [115]. For heat treatment above 12 h at 350 °C, the hematite/ITO samples showed negligible photo activity attributed to electrical conductivity loss by the ITO substrate under prolonged heat exposure. A more cathodic potential shift was observed as the time for heat treatment increased from 0, 3, 6, and 12 h and were recorded as 1.28, 1.19, 1.13, and 1.08 V vs RHE respectively. In addition, an increased donor density for hematite/ITO at 12 h was recorded at 2.52×10^{18} cm^{-3} compared to that at 2.28×10^{18} cm^{-3} for 0-h exposure [115]. A higher donor density implies reduced photo-generated charge recombination [116]. When the same experiment was carried out on FTO substrates, a similar cathodic potential shift was observed for increased heat treatment time 0 to 12 h of exposure [115]. This indicates that the substrate type does not affect the observed onset potential obtained for hematite thin films. Table 4 shows the various findings of research on ITO/pristine hematite photo-anodes.

Table 3 Work done on FTO/Hematite in Tandem PEC cell configuration

Device architecture	Surface morphology	Photocurrent density, J (mAcm^{-2}) taken under 1 sun at 1.23 V vs RHE	Flat band potential, V_{fb} (V) vs Ag/AgCl	Donor density, N_d ($\times 10^{19}$) (cm^{-3})	Performance efficiency (%) (taken in the range of 350–450 nm irradiation with an applied potential window from 0.50–1.80 V)	References
Ti:Fe$_2$O$_3$/FTO	Nano-particles	1.02			10.8 (IPCE)	[18]
Ti:Fe$_2$O$_3$/NTO/FTO	Nano-bowls filters	2.39			21.1 (IPCE)	[18]
Co-Pi/Ti:Fe$_2$O$_3$/NTO/FTO	Nano-spikes and Nano-cones on Nano-bowls filters	3.16			41.0 (IPCE)	[18]

Table 4 Work done on ITO/hematite/Electrolyte/Pt Configuration

Device architecture	Surface morphology	Photocurrent density, J (mAcm^{-2}) taken under 1 sun at 1.23 V vs RHE	Flat band potential, V_{fb} (V) vs Ag/AgCl; RHE	Donor density, N_d (×10^{19}) (cm^{-3})	Performance efficiency (%) (taken in the range of 350–450 nm irradiation with an applied potential window from 0.50–1.80 V)	References
α-Fe$_2$O$_3$/ITO	Mono-layered Nano-particles	0.032	−0.07	0.13	0.02 (ABPE)	[117]
Fe$_2$O$_3$/ITO	Uniformly distributed grains with inter-particle pores	0.22	0.9		5 (IPCE) 0.04 (Photo conversion efficiency)	[118]
Fe$_2$O$_3$/ITO		0.12	0.48	8.0		[119]
α-Fe$_2$O$_3$/ITO	Interconnected Nano-porous network	1.04	−0.45	31.7	0.65 (ABPE)	[120]
Fe$_2$O$_3$/ITO	Smooth Nano-sheets	0.217				[121]

5.4.2 ITO/hematite heterojunction/electrolyte/Pt

The annealing treatment given to a hetero-structure of hematite on ITO substrate has an impact on the properties realized of the heterojunction formed. In a study conducted by Palmolahti et al., the effect of annealing on $TiO_2/\alpha\text{-}Fe_2O_3/ITO$ material was carried out [119]. XPS results after annealing indicated that the Fe $2p_{3/2}$ binding energy peak shapes were unchanged due to the presence of Fe^{3+} oxidation states. On the other hand, the Ti^{4+} $2p_{3/2}$ binding energy peaks showed a -0.31 eV shift with reduced width size after annealing. The concentration of Ti at annealing temperatures above 500 °C was reduced well as that for In and Sn was increased—an indication of diffusion of Ti in the hematite top layer resulting in the formation of Fe^{3+} Ti^{4+} surface oxide. The researchers argue that much as In and Sn diffuse into hematite at high annealing temperatures, their binding energy peaks corresponding to In $3d_{5/2}$ and Sn $3d_{5/2}$ are unchanged—an indication of a stable chemical environment of hematite/ITO. In and Sn can diffuse from ITO into hematite at high annealing temperatures (above 500 °C) thus oxygen vacancies can be created on the surface of hematite [119, 120, 122]. Table 3 shows the various hetero-structure performances realized with hematite on ITO glass substrates.

Diab and Mokari managed to grow a uniform layer of magnetite (Fe_3O_4) on an ITO glass substrate by thermal decomposition of Fe(ac)z in an inert environment at 270 °C for 15 min sintered at 400 °C for 5 h followed by annealing at 700 °C for 12 min hence converting the Nanoporous magnetite into hematite (Fe_2O_3) mesoporous film [17]. In the study, modified hematite/CoO films were also synthesized by thermal decomposition followed by drop casting the mesoporous hematite films with $Co(NO_3)_2$ solution. A photocurrent density of 0.11 mAcm^{-2} at 1.82 V vs RHE was recorded for mesoporous hematite without any surface modification with an offset potential of 1.6 V vs RHE. Photocurrent densities of 1.17 mAcm^{-2} and 0.66 mAcm^{-2} were recorded for CoO-modified hematite and $Co(NO_3)_2$ modified hematite films respectively. The CoO-modified hematite film also exhibited a cathodic onset potential of 130 mV at 1.82 V vs RHE well as the $Co(NO_3)_2$ modified hematite film showed an onset potential shift of 70 mV at 1.82 V vs RHE which shows a significant improvement attributed to surface trap passivation in the modified films [17].

In another study, the $TiO_2/Fe_2O_3/ITO$ hetero-structure, its intermediate surface states (i-ss), and recombination surface states (r-ss) were studied at different annealing temperatures (300–700 °C) [119]. At an annealing temperature of 300 °C, the least recombination of free charge carriers was recorded in addition to having the highest population of r-ss at a delay time of 1 ns hence resulting in better PEC performance as shown in Fig. 8a (ii). The researchers also highlighted that the TiO_2 layer on hematite modifies its r-ss and hence improves on charge carrier life-time thus more will take part in the reaction processes for water splitting. Yu et al. compared the performance of pristine hematite on an ITO with that when an FeOOH layer is deposited on hematite forming $FeOOH/Fe_2O_3/ITO$ photo-anode [121]. Here, a photocurrent density of 217 µAcm^{-2} for Fe_2O_3/ITO photo-anode was recorded which turns into 850 µAcm^{-2} when decorated with FeOOH as a co-catalyst to form $FeOOH/Fe_2O_3/ITO$ as indicated in Fig. 8b (ii). This improvement is attributed to the small resistance to charge flow offered at the FeOOH-electrolyte interface which results in a positive effect to charge transfer at the interface. This is because the charge transfer barrier is reduced hence enhancing PEC performance. In another study, a CZTS p-type semiconductor with $\alpha\text{-}Fe_2O_3$ an n-type formed a p–n junction as shown in Fig. 8c (i) after band bending to match the Fermi levels of the semiconductors which led to the generation of an electric field that enables the charge carrier separation process [120]. The graph shown in Fig. 8c (ii) shows a comparative performance of the pristine Hematite/ITO (H), Hematite-Graphene/ITO (HG), CZTS QDs/Hematite/ITO (HC), and CZTS QDs/Hematite-Graphene/ITO (HGC) thin films at water splitting. High vacancy and low vacancy hematite were built to form the $HV/LV\text{-}Fe_2O_3$ junction where an electric field forms enabling accumulation of holes on the $LV\text{-}Fe_2O_3$ side which take part in the oxidation reaction at the Ohmic contact between the ITO substrate and the electrolyte hence the realized better PEC performance of the $HV/LV\text{-}Fe_2O_3/ITO$ photo-anode compared to the $LV\text{-}Fe_2O_3/ITO$ and the $HV\text{-}Fe_2O_3/ITO$ photo-anodes as shown in Fig. 8d (ii) [112]. Table 5 shows other studies carried out on hematite heterostructures set up in an ITO/Hematite heterojunction/Electrolyte/Pt configuration.

5.4.3 ITO/hematite tandem configuration

A $FeNiOOH/Fe_2TiO_5/Fe_2O_3/ITO$ photo-anode was built for use in a Tandem PEC cell set-up as shown in Fig. 9a [123]. Here, the thin film silicon photocathode together with the Ni-based catalyst powers the Tandem set-up. No external bias was used in the set-up yet a photocurrent density of 2.2 mAcm^{-2} was realized as indicated in Fig. 9b. Table 6 shows the PEC performance realized from the study's Tandem configuration.
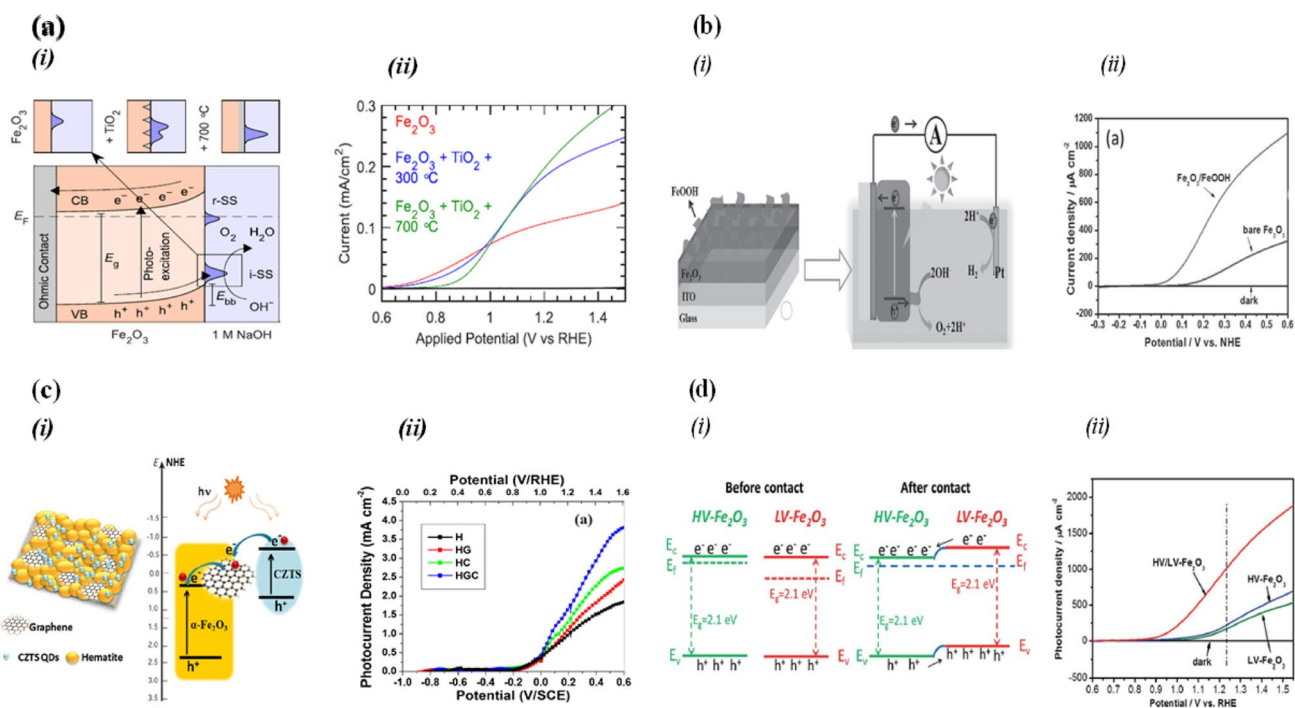
Fig. 8 Images of schematic diagrams showing hetero-structure build-ups and their corresponding photocurrent density comparisons with pristine hematite photo-anode performances on ITO glass substrates in photo-absorber photoanode/photo-absorber photocathode configuration (Adopted with permission **a** [119] copyright 2020, ACS Publications, **b** [112] copyright 2016, Royal Society of Chemistry, **c** [120] copyright 2022, Elsevier, **d** [121] copyright 2015, Willey)

5.5 PEC performance of hematite on other substrate types

Noble metal films like Pt films are recommended for use as substrates in times when high temperatures in addition to long sintering time, however, optical properties such as transparency may be affected [81]. These affect the nanostructure formed of hematite on deposition and hence affect the PEC performance of the structure formed. In a study conducted by Koziot-Rachwal et al. on the magnetic properties exhibited by hematite/Pt (111) hetero-structure, hematite was grown onto a Pt (111) seed layer by oxidation of magnetite (Fe_3O_4) (111) films [124]. Here exposure of Fe_3O_4 layers to oxygen at a pressure and high temperature (3×10^{-5} mbar and 770 K respectively) was done during the annealing process for 30 min after which magnetite turned into hematite (Fe_2O_3).

Fe substrates like Fe rods and Fe foils are also used as substrates over which hematite is deposited [31]. When an iron substrate was used, Nano-flakes were grown onto the iron substrate. On introducing Pt and FeOOH, a hetero-structure photo-anode of FeOOH/α-Fe_2O_3 NFs/Pt/iron substrate was formed which resulted in a cathodic photocurrent density of -2 mAcm^{-2}, a better photo-response compared to the α-Fe_2O_3 nFs/iron substrate photo-anode as shown in Fig. 10a (ii) [125]. In a CuO/α-Fe_2O_3/Fe-foil photo-anode, other than changing the surface morphology of the photo-anode from Nano-flakes to a coral-like morphology, the presence of a CuO layer forms a p–n junction resulting in an improved photocurrent density to a tune of 1.5 mAcm^{-2} from 0.7 for pristine hematite grown on a Fe-foil at a 1.6 V applied potential as shown in Fig. 10b (ii) [10].

Table 7 illustrates the different research works done on hematite hetero-structures on other substrates.

Table 5 Various works done on ITO/Hematite heterojunction/Electrolyte/Pt configuration

| Device architecture	Surface morphology	Photocurrent density, J (mAcm⁻²) taken under 1 sun at 1.23 V vs RHE	Flat band potential, V_{fb} (V) vs Ag/AgCl; RHE	Donor density, N_d ($\times 10^{19}$) (cm⁻³)	Performance efficiency (%) (taken in the range of 350–450 nm irradiation with an applied potential window from 0.50–1.80 V)	References
α-Fe$_2$O$_3$/ZnO/ITO	Bi-layered Nano-hetero-structure	0.218	0.25	0.20	0.10 (ABPE)	[117]
Ag-α-Fe$_2$O$_3$/ZnO/ITO	Bi-layered Nano-hetero-structure with rough surface	0.658	0.14	0.18	0.32 (ABPE)	[117]
TiO$_3$/Fe$_2$O$_3$/ITO	Double layered inter-particles	2.10	0.2		10 (IPCE) 1.13 (Photo conversion efficiency)	[118]
H:TiO$_3$/Fe$_2$O$_3$/ITO	Double layered inter-particles	3.56	0.1		24.5 (IPCE) 1.68 (Photo conversion efficiency)	[118]
TiO$_2$/Fe$_2$O$_3$/ITO		0.30	0.48	15.0		[119]
FeOOH/Fe$_2$O$_3$/ITO	Rough Nano-sheets with ribbons (Rugged surface)	0.850			20.2 (IPCE)	[121]
Cu$_2$ZnSnS$_4$QDs/α-Fe$_2$O$_3$-Grapnene/ITO	Nano-porous structure in clusters	1.80	0.04	13.7	1.10 (ABPE)	[120]
Cu$_2$ZnSnS$_4$QDs/α-Fe$_2$O$_3$/ITO	Nano-porous structure	1.47	0.04	11.1	0.9 (ABPE)	[120]
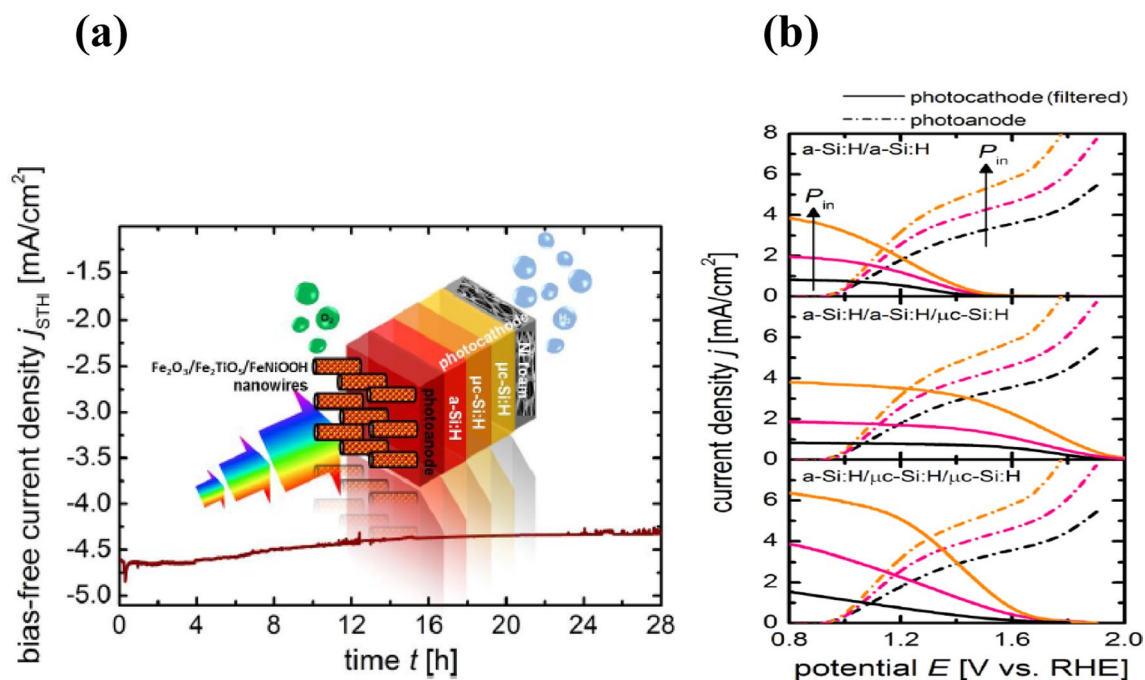
Fig. 9 Images of schematic diagrams showing **a** a hetero-structure build-up and **b** the corresponding photocurrent density comparisons with pristine hematite photo-anode performances on ITO glass substrates in tandem cell configuration (Adopted with permission [123] copyright 2019, Willey)

6 Conclusion and outlook

The single photoanode light absorber and the heterojunction semiconductor photoanode light absorber configurations are the commonly used PEC device configurations in hematite studies. Pt is the common counter electrode used citing its electrocatalytic property which helps in reducing mass-transport over-potential [128]. All PEC device configurations require Ohmic contacts where the electronic junction is formed [129]. Hematite's PEC water-splitting performance is still low due to its poor C.B edge match with the H_2O reduction potential. Much as the series connected photoanode and photocathode (Tandem) PEC device configurations enable bias-free PEC cell operation, challenges of limited light absorption and low current density are still hindering their performance [36]. From the reviewed studies, the best photoanode light absorber configuration performance is at a photocurrent density of 3.56 mAcm^{-1} with a heterojunction photo-anode of H:TiO_3/Fe_2O_3/ITO, and 4.2 mAcm^{-1} for Tandem configuration obtained from μc-Si:H/μc-Si:H/α-Fe_2O_3/ITO which is bias-free [118, 123]. Formation of a homo-junction between hematite and ITO leads to improved absorption of the sun's photo energy [111]. Formation of a heterostructure increases the donor density and leads to positive shift in the flat band potential and results in band bending at the heterojunction interfaces improving on the charge separation [1]. Also surface catalysis exhibited by heterojunction photo-electrodes enables the material to perform better at charge separation in the bulk as well as increases on its charge carrier concentration [85]. The best Hematite/FTO performance is at a photocurrent density of 1.02 mAcm^{-1} in Tandem configuration, 1.04 mAcm^{-1} for Hematite/ITO in single photoanode light absorber configuration, and 2.8 mAcm^{-1} for Hematite/Ceramic in single photoanode light absorber configuration [18, 120, 127]. An indication that substrates affect the hematite's PEC performance in different PEC device configurations.

Conducting substrates are used to form PEC photo-electrodes and preference is given to TCOs since these enable creation of an Ohmic contact which enhances transportation of charge carriers—the reason for the common use of FTO and ITO substrates [81]. Transparent substrates also provide for both back-side and front-side illumination. Front-side illumination reduces on the length the holes have to diffuse after photo-activity to take part in the reaction process well as back-side illumination reduce on the electrons' length traveled without moving through the bulk of the electrode [48]. Therefore, balancing of hematite's thickness with light absorption to favor particular charge carrier transportation is necessary.

Discover

Table 6 Various works done on hematite hetero-structures in an ITO/Hematite Tandem Configuration

Device architecture	Surface morphology	Photocurrent density, J (mAcm^{-2}) taken under 1 sun at 1.23 V vs RHE	Flat band potential, V_{fb} (V) vs Ag/AgCl; RHE	Donor density, N_d ($\times 10^{19}$) (cm^{-3})	Performance efficiency (%) (taken in the range of 350–450 nm irradiation with an applied potential window from 0.50–1.80 V)	References
ac-Si:H/a-Si:H/α-Fe$_2$O$_3$/ITO	Multi-layer Nano-wires	2.5			1.00 (S.T.H)	[123]
μc-Si:H/μc-Si:H/α-Fe$_2$O$_3$/ITO	Multi-layer Nano-wires	4.2			1.72 (S.T.H)	[123]
μc-Si:H/ac-Si:H/α-Fe$_2$O$_3$/ITO	Multi-layer Nano-wires	3.0			1.25 (S.T.H)	[123]
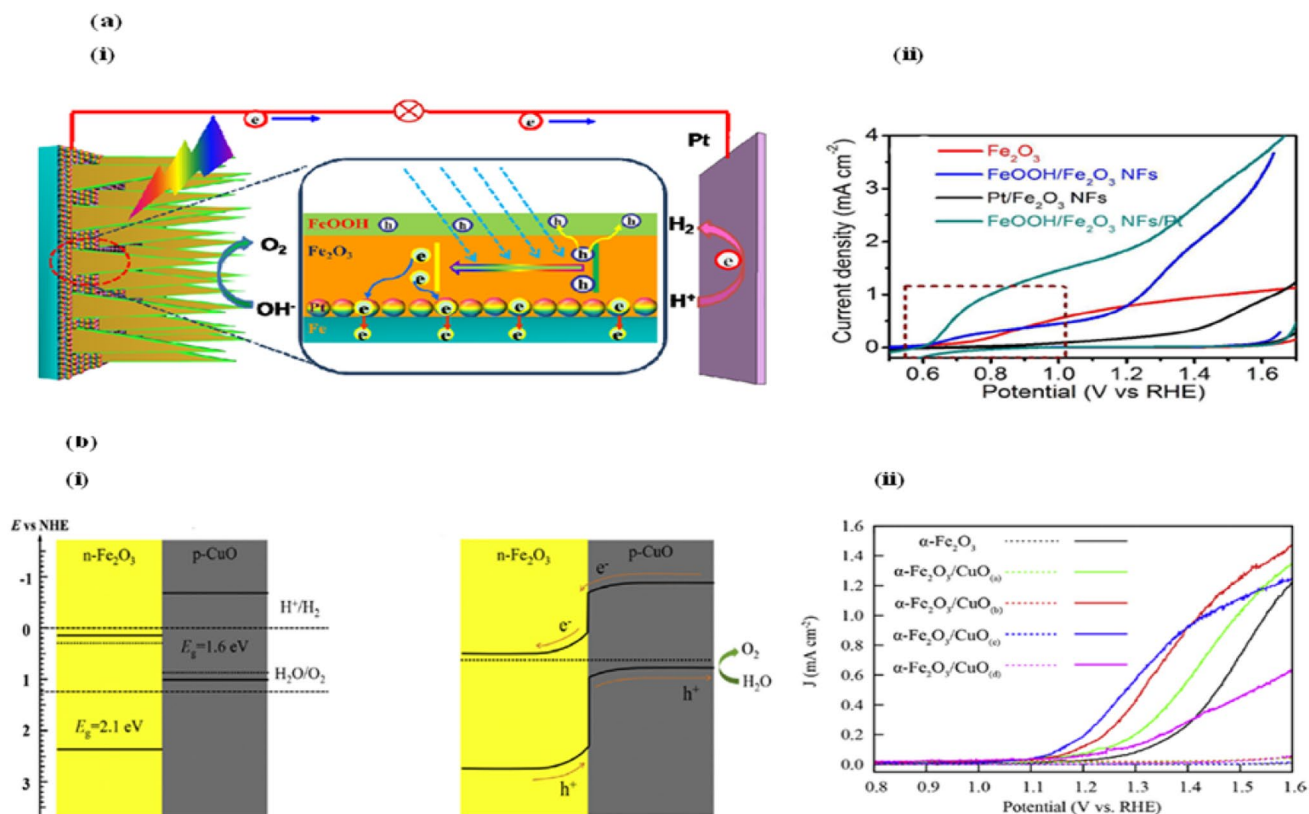
Fig. 10 Schematic diagrams showing performances of hematite photo-anode hetero-structure and their corresponding photocurrent density in comparisons with pristine hematite on other substrates (Adopted with permission **a** [125] copyright 2017, RSC Publishing and **b** [10] copyright 2020, Elsevier)

As much as longer annealing time at higher annealing temperatures leads to reduced recombination centers in a hematite electrode, care has to be taken on the substrate used. This is because FTO substrates may deform in addition to Sn^{4+} cations diffusing into hematite resulting in doping hematite with Sn, well as for an ITO substrate, the electrical conductivity is lost [81].

More studies on the performance of hematite hetero-structures on an ITO substrate in a Tandem configuration (bias-free) with a suitable membrane can be focused on aiming at improving light absorption to enhance hematite's PEC performance.

Research on hematite photo-anodes for other photoelectrocatalytic reactions like the production of H_2O_2, degradation of organic pollutants and organic synthesis can be explored.

Furthermore, the introduction of out-fields like magnetic and photothermal fields can be explored to enhance the PEC efficiency of hematite.

Table 7 Various works done on pristine hematite and hetero-structures on other substrates

Device architecture	Surface morphology	Photocurrent density, J (mAcm^{-2}) taken under 1 sun at 1.23 V vs RHE	Flat band potential, V$_{fb}$ (V) vs Ag/AgCl; RHE	Donor density, N$_d$ ($\times 10^{19}$) (cm^{-3})	Performance efficiency (%) (taken in the range of 350–450 nm irradiation with an applied potential ranging from 0.50–1.80 V)	References
Sustrate/pristine hematite heterojunction/electrolyte/Pt configuration						
α-Fe$_2$O$_3$/Fe-foil	Nano-flakes	0.7				[10]
α-Fe$_2$O$_3$/Ti-foil	Non homogeneous Nano-pillars with different diameters	0.60				[126]
Sustrate/hematite heterojunction/electrolyte/Pt configuration						
α-Fe$_2$O$_3$/SnO$_2$-Sb$_2$O$_5$ ceramic substrate	Porous grains	2.8			3.8 (IPCE)	[127]
CuO/α-Fe$_2$O$_3$/Fe-foil	Coral-like	1.5				[10]
α-Fe$_2$O$_3$/TiO$_2$/Ti-foil	Non-homogeneous Nano-pillars	1.40				[126]

Data availability No datasets were generated or analysed during the current study.

Declarations

Competing interests The authors declare no competing interests.

References

1. Farhoosh S, Eftekharinia B, Tayebi M, Lee B, Naseri N. Newly designed ternary hematite-based heterojunction for PEC water splitting. Appl Surf Sci. 2021;550(1–10): 149374. https://doi.org/10.1016/j.apsusc.2021.149374.
2. Peng Q, Wang J, Feng Z, Du C, Wen Y, Shan B, Chen R. Enhanced photoelectrochemical water oxidation by fabrication of p-LaFeO3/n-Fe2O3 heterojunction on hematite nanorods. J Phys Chem. 2017;121:12991–8. https://doi.org/10.1021/acs.jpcc.7b01817.
3. Najaf Z, Nguyen DLT, Chae SY, Joo O-S, Shah AUHA, Vo D-VN, Nguyen V-H, Van Le Q, Rahman G. Recent trends in development of hematite (a-Fe2O3) as an efficient photoanode for enhancement of photoelectrochemical hydrogen production by solar water splitting. Int J Hydrogen Energy. 2020;46:23334–57. https://doi.org/10.1016/j.ijhydene.2020.07.111.
4. Shen S, Lindley SA, Chen X, Zhang JZ. Hematite heterostructures for photoelectrochemical water splitting: rational materials design and charge carrier dynamics. Energy Environ Sci. 2016;9:2744–75. https://doi.org/10.1039/C6EE01845A.
5. Tamirat AG, Rick J, Dubale AA, Su WN, Hwang BJ. Using hematite for photoelectrochemical water splitting: a review of current progress and challenges. Nanoscale Horizons. 2016;1:243–67. https://doi.org/10.1039/c5nh00098j.
6. Bouhjar F, Guaita JM, Mittal A. Development of metal oxide heterostructures for hydrogen production. In: Met. oxide-based heterostruct. London: Elsevier Inc.; 2023. p. 501–33. https://doi.org/10.1016/B978-0-323-85241-8.00012-8.
7. Liu J, Shahid M, Ko Y-S, Kim E, Ahn TK, Park JH, Kwon Y-U. Investigation of porosity and heterojunction effects of a mesoporous hematite electrode on photoelectrochemical water splitting. Phys Chem Chem Phys. 2013;15:9775–82. https://doi.org/10.1039/c3cp51053k.
8. Zhang H, Kim YK, Jeong HY, Lee JS. A few atomic FeNbO4 overlayers on hematite nanorods: microwave-induced high temperature phase for efficient photoelectrochemical water splitting. ACS Catal. 2019;9:1289–97. https://doi.org/10.1021/acscatal.8b04034.
9. Li F, Jian J, Xu Y, Wang S, Wang H, Wang H. Recent advances on interfacial engineering of hematite photoanodes for viable photoelectrochemical water splitting. Eng Reports. 2021;3(e12387):1–32. https://doi.org/10.1002/eng2.12387.
10. Zhu C, Li C, Miao X, Zhao L, Wang Z, Delaunay J. Photoelectrochemical water oxidation performance promoted by a cupric oxide-hematite heterojunction photoanode. Sci Direct Int J Hydrog Energy. 2020;45:33102–10. https://doi.org/10.1016/j.ijhydene.2020.09.091.
11. Shen S. Toward efficient solar water splitting over hematite photoelectrodes. J Mater Chem A. 2014;29:29–46. https://doi.org/10.1557/jmr.2013.310.
12. Ashraf M, Khan I, Usman M, Khan A, Shah SS, Khan AZ, Saeed K, Yaseen M, Ehsan MF, Tahir MN, Ullah N. Hematite and magnetite nanostructures for green and sustainable energy harnessing and environmental pollution control: a review. Chem Res Toxicol Am Chem Soc Publ. 2020;33:1292–311. https://doi.org/10.1021/acs.chemrestox.9b00308.
13. Bao Z, Sun Z, Li Z, Tian L, Ngai T, Wang J. Plasmonic gold À superparamagnetic hematite heterostructures. Langmuir Am Chem Soc. 2011;27:5071–5. https://doi.org/10.1021/la200147d.
14. Zhang Q, Han P, Mei J. Interfacial design on grapheme—hematite heterostructures for enhancing adsorption and diffusion towards superior lithium storage. Nano Mater. 2021;11:81. https://doi.org/10.3390/nano11010081.
15. Kim S. Editorial of special issue "materials for energy applications 2.0." Int J Mol Sci. 2023;24:4892.
16. Zhang Z, Tsuchimochi T, Ina T, Kumabe Y, Muto S, Ohara K, Yamada H, Ten-no SL, Tachikawa T. Binary dopant segregation enables hematite-based heterostructures for highly efficient solar H2O2 synthesis. Nat Commun. 2022;13:1499. https://doi.org/10.1038/s41467-022-28944-y.
17. Diab M, Mokari T. Thermal decomposition approach for the formation of α-Fe2O3 mesoporous photoanodes and an α-Fe2O3/CoO hybrid structure for enhanced water oxidation. Inorg Chem. 2014;53:2304–9. https://doi.org/10.1021/ic403027r.
18. Yan K, Qiu Y, Xiao S, Gong J, Zhao S, Xu J, Meng X, Yang S, Xu J. Self-driven hematite-based photoelectrochemical water splitting cells with three-dimensional nanobowl heterojunction and high-photovoltage perovskite solar cells. Mater Today Energy. 2017;6:128–35. https://doi.org/10.1016/j.mtener.2017.09.006.

Discover

19. Tsege LE, Atebaev ST, Hossain MA, Lee D, Kim H-K, Hwang Y-H. Cu-doped flower-like hematite nanostructures for efficient water splitting applications. J Phys Chem Solids. 2016;98:283–9. https://doi.org/10.1016/j.jpcs.2016.07.014.

20. Bahadoran A, Liu Q, Ramakrishna S, Sadeghi B, De Castro MM, Cavaliere PD. Hydrogen production as a clean energy carrier through heterojunction semiconductors for environmental remediation. Energies. 2022;15:3222. https://doi.org/10.3390/en15093222.

21. Wan H, Hu L, Liu X, Zhang Y, Chen G, Zhang N, Ma R. Advanced hematite nanomaterials for newly emerging applications. Chem Sci. 2023;14:2776–98. https://doi.org/10.1039/d3sc00180f.

22. Krehula S, Ristic M, Reissner M, Kubuki S, Music S. Synthesis and properties of indium-doped hematite. J Alloys Compd. 2017;695:1900–7. https://doi.org/10.1016/j.jallcom.2016.11.022.

23. Kment S, Riboni F, Pausova S, Wang L, Wang L, Han H, Hubicka Z, Krysa J, Schmuki P, Zboril R. Photoanodes based on TiO2 and a-Fe2O3 for solar water splitting – superior role of 1D nanoarchitectures and of combined heterostructures. Chem Soc Rev. 2017;46:3716–69. https://doi.org/10.1039/C6CS00015K.

24. Kormányos A, Kecsenovity E, Honarfar A, Pullerits T, Janáky C. Hybrid FeNiOOH/α-Fe2O3/graphene photoelectrodes with advanced water oxidation performance. Adv Funct Mater. 2020;30:2002124. https://doi.org/10.1002/adfm.202002124.

25. Song A, Bogdano P, Esau A, Ahmet IY, Levine I, Dittrich T, Unold T, Van De Krol R, Berglund SP. Assessment of a W:BiVO4–CuBi2O4 tandem photoelectrochemical cell for overall solar water splitting. ACS Appl Mater Interfaces. 2020;12:13959–70. https://doi.org/10.1021/acsami.0c00696.

26. Song A, Berglund SP, Chemseddine A, Friedrich D, Abdi FF, Van-de-Krol R. Elucidating the optical, electronic, and photoelectrochemical properties of p-type copper vanadate (p-Cu5V2O10) photocathodes. J Mater Chem A. 2020;8:12538–47. https://doi.org/10.1039/d0ta04250a.

27. Song A, Plate P, Chemseddine A, Wang F, Abdi FF, Wollgarten M, Van-de-Krolab R, Berglunda SP. Cu:NiO as a hole-selective back contact to improve the photoelectrochemical performance of CuBi2O4 thin film photocathodes. J Mater Chem A. 2019;7:9183–94. https://doi.org/10.1039/C9TA01489F.

28. Song A, Chemseddine A, Ahmet IY, Bogdano P, Friedrich D, Abdi FF, Berglund SP, Van De Krol R. Evaluation of copper vanadate (β-Cu2V2O7) as a photoanode material for photoelectrochemical water oxidation. Chem Mater. 2020;32:2408–19. https://doi.org/10.1021/acs.chemmater.9b04909.

29. Song A, Levine I, Van-de-Krol R, Dittrich T, Berglund SP. Revealing the relationship between photoelectrochemical performance and interface hole trapping in CuBi2O4 heterojunction photoelectrodes. Chem Sci. 2020;11:11195–204. https://doi.org/10.1039/d0sc03030a.

30. Choudhary S, Upadhyay S, Kumar P, Singh N, Satsangi VR, Shrivastav R, Dass S. Nanostructured bilayered thin films in photoelectrochemical water splitting—a review. Int J Hydrogen Energy. 2012;37:18713–30. https://doi.org/10.1016/j.ijhydene.2012.10.028.

31. Phuan YW, Ongc W-J, Chong MN, Ocon JD. Prospects of electrochemically synthesized hematite photoanodes for photoelectrochemical water splitting: a review. J Photochem Photobiol C Photochem Rev. 2017;33:54–82. https://doi.org/10.1016/j.jphotochemrev.2017.10.001.

32. Esmaili H, Kowsari E, Ramakrishna S. Significance of nanostructure morphologies in photoelectrochemical water splitting cells: a brief review. J Mol Struct. 2021;1230: 129856. https://doi.org/10.1016/j.molstruc.2020.129856.

33. Saraswat KS, Rodene DD, Gupta RB. Recent advancements in semiconductor materials for photoelectrochemical water splitting for hydrogen production using visible light. Renew Sustain Energy Rev. 2018;89:228–48. https://doi.org/10.1016/j.rser.2018.03.063.

34. Iqbal MZ, Siddique S. Recent progress in efficiency of hydrogen evolution process based photoelectrochemical cell. Int J Hydrogen Energy. 2018;43:21502–23. https://doi.org/10.1016/j.ijhydene.2018.09.157.

35. Raza A, Zhang X, Ali S, Cao C, Rafi AA, Li G. Photoelectrochemical energy conversion over 2D materials. Photochem. 2022;2:272–98. https://doi.org/10.3390/photochem2020020.

36. Jun SE, Lee JK, Jang HW. Two-dimensional materials for photoelectrochemical water splitting. Energy Adv. 2023;2:34–53. https://doi.org/10.1039/d2ya00231k.

37. Li S, Xu W, Meng L, Tian W, Li L. Recent progress on semiconductor heterojunction-based photoanodes for photoelectrochemical water splitting. Small Sci J. 2022;2:2100112. https://doi.org/10.1002/smsc.202100112.

38. He H, Liao A, Guo W, Luo W, Zhou Y, Zou Z. State-of-the-art progress in the use of ternary metal oxides as photoelectrode materials for water splitting and organic synthesis. Nano Today. 2019;28: 100763. https://doi.org/10.1016/j.nantod.2019.100763.

39. Liao A, He H, Zhou Y, Zou Z. Typical strategies to facilitate charge transfer for enhanced oxygen evolution reaction: case studies on hematite. J Semicond. 2020;41: 091709. https://doi.org/10.1088/1674-4926/41/9/091709.

40. Ke GL, Jia B, He HC, Zhou Y, Zhou M. State-of-the-art advancements of transition metal oxides as photoelectrode materials for solar water splitting. Rare Met. 2022;41:2370–86. https://doi.org/10.1007/s12598-022-01968-5.

41. Ikeda S, Ishizuka S. Chalcopyrite CuGaSe 2 thin film for photoelectrochemical water splitting into hydrogen. JSAP Rev. 2023;92: 230413. https://doi.org/10.11470/jsaprev.230413.

42. Schleuning M, Ahmet IY, Van-de-Krol R, May MM. The role of selective contacts and built-in field for charge separation and transport in photoelectrochemical devices, Sustain. Energy Fuels. 2022;6:3701–16. https://doi.org/10.1039/d2se00562j.

43. Prévot MS, Sivula K. Photoelectrochemical tandem cells for solar water splitting. J Phys Chem C. 2013;117:17879–93. https://doi.org/10.1021/jp405291g.

44. Hejazi S, Altomare M, Schmuki P. photo-electrochemical solar-to-fuel energy conversion by hematite-based photo-anodes—the role of 1D nanostructuring 1 introduction. Z Phys Chem. 2020;234:615–31. https://doi.org/10.1515/zpch-2019-1479.

45. Zhang H, Liu J, Xu T, Ji W, Zong X. Recent advances on small band gap semiconductor materials (≤2.1 eV) for solar water splitting. Catalysts. 2023;13(10):728.

46. Jiang C, Moniz SJA, Wang A, Zhang T, Tang J. Photoelectrochemical devices for solar water splitting-materials and challenges. Chem Soc Rev. 2017;46:4645–60. https://doi.org/10.1039/c6cs00306k.

47. Chen L, Ren J-T, Yuan Z-Y. Enabling internal electric fields to enhance energy and environmental catalysis. Adv Energy Mater. 2023;13:2203720. https://doi.org/10.1002/aenm.202203720.

48. Smith WA. Photoelectrochemical cell design, efficiency, definitions, standards, and protocols. In: Giménez S, Bisquert J, editors. Photo-electrochemical solar fuel production: from basic principles to advanced devices. 1st ed. Cham: Springer; 2016. p. 163–97. https://doi.org/10.1007/978-3-319-29641-8.

49. Li J, Yuan H, Zhang W. Advances in Z—scheme semiconductor photocatalysts for the photoelectrochemical applications: a review. Carbon Energy. 2022;4:294–331. https://doi.org/10.1002/cey2.179.

50. Wierzbicka E, Schultz T, Sulka GD, Koch N, Syrek K, Pinna N. Ultra-stable self-standing Au nanowires/TiO2 nanoporous membrane system for high-performance photoelectrochemical water splitting cells. Mater Horizons. 2022;9:2797–808. https://doi.org/10.1039/d2mh00718e.

51. Licht S, Khaselev O, Ramakrishnan PA. Multiple-bandgap photoelectrochemistry: bipolar semiconductor ohmic regenerative electro-chemistry. J Phys Chem B. 1998;102:2536–45.

52. Licht S. Multiple band gap semiconductor/electrolyte solar energy conversion. J Phys Chem B. 2001;105:6281–94. https://doi.org/10.1021/jp010552j.

53. Mukhokosi EP, Krupanidhi SB, Nanda KK. An extrinsic approach toward achieving fast response and self-powered photodetector. Adv Sci News Phys Status Solidi A. 2018;215:1800470. https://doi.org/10.1002/pssa.201800470.

54. Mukhokosi EP, Roul B, Krupanidhi SB, Nanda KK. Toward a Fast and highly responsive SnSe 2—based photodiode by exploiting the mobility of the counter semiconductor. ACS Appl Mater Interfaces. 2019;11:6184–94. https://doi.org/10.1021/acsami.8b16635.

55. Mukhokosi EP, Maaza M. Influence of device architectures and mobility on response/recovery time of metal halide perovskites: a review. J Mater Sci. 2022. https://doi.org/10.1007/s10853-021-06678-4.

56. Mukhokosi EP, Manohar GVS, Nagao T, Krupanidhi SB, Nanda KK. Device architecture for visible and near-infrared photodetectors based on two-dimensional SnSe2 and MoS2: a review. Micromachines. 2020;11:1–30. https://doi.org/10.3390/MI11080750.

57. Lopes T, Dias P, Andrade L, Mendes A. Solar energy materials & solar cells an innovative photoelectrochemical lab device for solar water splitting. Sol Energy Mater Sol Cells. 2014;128:399–410. https://doi.org/10.1016/j.solmat.2014.05.051.

58. Kim H, Seo JW, Chung W, Narejo GM, Koo SW, Han JS, Yang J, Kim J-Y, In S-I. Thermal effect on photoelectrochemical water splitting toward highly solar to hydrogen efficiency. Chemsuschem. 2023;16: e202202017. https://doi.org/10.1002/cssc.202202017.

59. Jun SE, Lee JK, Jang HW. As featured. Energy Adv Energy Adv. 2023;2:34–53. https://doi.org/10.1039/d2ya00231k.

60. Sivula K, Le Formal F, Grätzel M. Solar water splitting: progress using hematite (a-Fe2O3) photoelectrodes. Chem Sus Chem. 2011;4:432–49. https://doi.org/10.1002/cssc.201000416.

61. Teja AS, Koh PY. Synthesis, properties, and applications of magnetic iron oxide nanoparticles. Sci Direct Prog Cryst Growth Charact Mater. 2009;55:22–45. https://doi.org/10.1016/j.pcrysgrow.2008.08.003.

62. Bassi PS, Gurudayal LH, Wong J. Barber, iron based photoanodes for solar fuel production. Phys Chem Chem Phys. 2014;16:11834–42. https://doi.org/10.1039/c3cp55174a.

63. Chernyshova IV, Ponnurangam S, Somasundaran P. Linking interfacial chemistry of CO2 to surface structures of hydrated metal oxide nanoparticles: hematite. Phys Chem Chem Phys. 2013;15:6953–64. https://doi.org/10.1039/c3cp44264k.

64. Ahmadipour M, Kian CW, Ain MF, Rao KV, Ahmad ZA. Effects of deposition temperatures and substrates on microstructure and optical properties of sputtered CCTO thin film. Mater Lett. 2018;210:4–7. https://doi.org/10.1016/j.matlet.2017.08.121.

65. Aouaj MA, Diaz R, Belayachi A, Rueda F, Abd-lefdil M. Comparative study of ITO and FTO thin films grown by spray pyrolysis. Mater Res Bull. 2009;44:1458–61. https://doi.org/10.1016/j.materresbull.2009.02.019.

66. Landolsi Z, Ben Assaker I, Chtourou R, Ammar S. Photoelectrochemical impedance spectroscopy of electrodeposited hematite α-Fe2O3 thin films: effect of cycle numbers. J Mater Sci Mater Electron. 2018;29:8176–87. https://doi.org/10.1007/s10854-018-8824-7.

67. Samad WZ, Salleh MM, Shafiee A, Yarmo MA. Structural, optical and electrical properties of fluorine doped tin oxide thin films deposited using inkjet printing technique. Sains Malaysiana. 2011;40:251–7.

68. S. Zhang, Study of fluorine-doped tin oxide (FTO) thin films for photovoltaics applications, Université Grenoble Alpes (UGA, France) and Technische Universität Darmstadt (TU Darmstadt, Germany); 2018. https://www.theses.fr/2017GREAI021%0A. https://tel.archives-ouvertes.fr/tel-01689976/document.

69. Bouhjar F, Ullah S, Chourou ML, Mollar M, Mari B, Bessais B. Electrochemical fabrication and characterization of p-CuSCN/n-Fe2O3 Heterojunction devices for hydrogen production. J Electrochem Soc. 2017;164:H936–45. https://doi.org/10.1149/2.1431713jes.

70. Kumar A, Yadav K. Optical properties of nanocrystallite films of α-Fe2O3 and α-Fe2−xCrxO3 (0.0 x 0.9) deposited on glass substrates. Mater Res Expr. 2017;4: 075003. https://doi.org/10.1088/2053-1591/aa75e9.

71. Ahmed MR, Ali HM, Hasaneen MF. Influence of different types of substrates on the physical properties of CdSe films. Phys B Phys Condens Matter. 2021;608: 412747. https://doi.org/10.1016/j.physb.2020.412747.

72. Sanson A, Mathon O, Pascarelli S. Local vibrational dynamics of hematite (α-Fe2O3) studied by extended x-ray absorption fine structure and molecular dynamics. J Chem Phys. 2014;140: 224504. https://doi.org/10.1063/1.4882282.

73. Choi Y, Lee H, Kumbhar VS, Choi Y, Kim J, Lee K. Enhancement of photoelectrochemical properties with α-Fe2O3 on surface modified FTO substrates. Ceram Int. 2020;46:20012–9. https://doi.org/10.1016/j.ceramint.2020.05.072.

74. Eftekharinia B, Moshaii A, Dabirian A. Optimization of charge transport in a Co-Pi modified hematite thin film produced by scalable electron beam evaporation for photoelectrochemical water oxidation. J Mater Chem A. 2017;5:3412–24. https://doi.org/10.1039/C6TA09331K.

75. Liccardo L, Lushaj E, Compare LD, Moretti E, Vomiero A. Nanoscale ZnO/α-Fe2O3 heterostructures: toward efficient and low-cost photoanodes for water splitting. Small Sci. 2022. https://doi.org/10.1002/smsc.202100104.

76. Pan H, Meng X, Liu D, Li S, Qin G. (Ti/Zr, N) codoped hematite for enhancing the photoelectrochemical activity of water splitting. Phys Chem Chem Phys. 2015;17:22179–86. https://doi.org/10.1039/C5CP01489A.

77. Ling Y, Li Y. Review of Sn-doped hematite nanostructures for photoelectrochemical water splitting. Part Part Syst Charact. 2014;31:1113–21. https://doi.org/10.1002/ppsc.201400051.

78. Sharma D, Upadhyay S, Verma A, Satsangi VR, Shrivastav R, Dass S. Nanostructured Ti-Fe2O3/Cu2O heterojunction photoelectrode for efficient hydrogen production. Thin Solid Films. 2014;574:125–31. https://doi.org/10.1016/j.tsf.2014.12.003.

79. Li M, Zhang Z, Lyu F, He X, Liang Z, Balogun M-S, Lu X, Fang P-P, Tong Y. Facile hydrothermal synthesis of three dimensional hematite nanostructures with enhanced water splitting performance. Electrochim Acta. 2015;186:95–100. https://doi.org/10.1016/j.electacta.2015.10.048.

80. Li J, Qiu Y, Wei Z, Lin Q, Zhang Q, Yan K, Chen H, Xiao S, Fan Z, Yang S. A three-dimensional hexagonal fluorine-doped tin oxide nanocone array: a superior light harvesting electrode for high performance photoelectrochemical water splitting. Energy Environ Sci. 2014;7:3651–8. https://doi.org/10.1039/C4EE01581A.

81. Annamalai A, Subramanian A, Kang U, Park H, Choi SH, Jang JS. Activation of hematite photoanodes for solar water splitting: effect of FTO deformation. J Phys Chem C. 2015. https://doi.org/10.1021/jp512189c.

82. Myat S, Htay T, May Y, Nyein Khine S, Kyawt NK. Determination of semiconductor type and optical properties of SnO2:F(FTO) and SnO2:In(ITO). Int J Sci Res Publ. 2019;9:558–63. https://doi.org/10.29322/ijsrp.9.02.2019.p8671.

83. Li C, Luo Z, Wang T, Gong J. Surface, bulk, and interface: rational design of hematite architecture toward efficient photo-electrochemical water splitting. Adv Mater. 2018;30:1707502. https://doi.org/10.1002/adma.201707502.

84. Bisht H, Eun H, Mehrtens A, Aegerter MA. Comparison of spray pyrolyzed FTO, ATO and ITO coatings for flat and bent glass substrates. Thin Solid Films. 1999;351:109–14.

85. Zhang H, Li P, Zhou H, Xu J, Jiang Q, Hadden JHL, Wang Y, Wang M, Chen S, Xie F, Riley DJ. Unravelling the synergy of oxygen vacancies and gold nanostars in hematite for the electrochemical and photoelectrochemical oxygen evolution reaction. Nano Energy. 2022;94: 106968. https://doi.org/10.1016/j.nanoen.2022.106968.

86. Guo Q, Zhao Q, Crespo-otero R, Di Tommaso D, Tang J, Dimitrov SD, Titirici M, Li X, Sobrido ABJ. Single-atom iridium on hematite photoanodes for solar water splitting: catalyst or spectator? J Am Chem Soc. 2023;145:1686–95. https://doi.org/10.1021/jacs.2c09974.

87. Ahmed MG, Kandiel TA, Ahmed AY, Rashwan FA, Bahnemann DW. Enhanced photoelectrochemical water oxidation on hematite photoanode via p-CaFe2O4/n-Fe2O3 heterojunction formation. J Phys Chem. 2015;119:5864–71. https://doi.org/10.1021/jp512804p.

88. Masoumi Z, Tayebi M, Kolaei M, Lee B. Unified surface modification by double heterojunction of MoS2 nanosheets and BiVO4 nanoparticles to enhance the photoelectrochemical water splitting of hematite photoanode. J Alloys Compd. 2021;890: 161802. https://doi.org/10.1016/j.jallcom.2021.161802.

89. Ma J, Wang Q, Li L, Zong X, Sun H, Tao R, Fan X. Fe2O3 nanorods /CuO nanoparticles p-n heterojunction photoanode: effective charge separation and enhanced photoelectrochemical properties. J Colloid Interface Sci. 2021;602:32–42. https://doi.org/10.1016/j.jcis.2021.05.140.

90. Tokubuchi T, Arbi RI, Zhenhua P, Katayama K, Turak A, Sohn WY. Enhanced photoelectrochemical water splitting efficiency of hematite (α -Fe2O3)-based photoelectrode by the introduction of maghemite. J Photochem Photobiol A Chem. 2021;410: 113179. https://doi.org/10.1016/j.jphotochem.2021.113179.

91. Alhabradi M, Nundy S, Ghosh A, Tahir AA. Vertically aligned CdO-decked α-Fe2O3 nanorod arrays by a radio frequency sputtering method for enhanced photocatalytic applications. ACS Omega. 2022;7:28396–283407. https://doi.org/10.1021/acsomega.2c02996.

92. Gedamu A, Su W, Dubale AA, Pan C, Chen H, Ayele DW, Lee J, Hwang B. Efficient photoelectrochemical water splitting using three dimensional urchin-like hematite nanostructure modified with reduced graphene oxide. J Power Sources. 2015;287:119–28. https://doi.org/10.1016/j.jpowsour.2015.04.042.

93. Bouhjar F, Marí B, Bessaïs B. Hydrothermal fabrication and characterization of ZnO/Fe2O3 heterojunction devices for hydrogen production. J Anal Pharm Res. 2018;7:315–21. https://doi.org/10.15406/japlr.2018.07.00246.

94. Kyesmen PI, Nombona N, Diale M. Heterojunction of nanostructured α-Fe2O3/CuO for enhancement of photoelectrochemical water splitting. J Alloys Compd. 2021;863: 158724. https://doi.org/10.1016/j.jallcom.2021.158724.

95. Wu Q, Liang X, Chen H, Yang L, Xie T, Zou X. Surface-oxidized titanium diboride as cocatalyst on hematite photoanode for solar water splitting. CrystEngComm. 2022;24:2251–7. https://doi.org/10.1039/d2ce00122e.

96. Shi T, Feng Y, Zhong Y, Ding H, Chen K, Chen D. In situ synthesis of Ti: Fe2O3/Cu2O p-n junction for highly efficient photogenerated carriers separation. Inorganics. 2023;11:155. https://doi.org/10.3390/inorganics11040155.

97. Tang P, Xie H, Ros C, Han L, Biset-Peiró M, He Y, Kramer W, Rodríguez AP, Saucedo E, Mascarós JRG, Andreu T, Morante JR, Arbiol J. Enhanced photoelectrochemical water splitting of hematite multilayer nanowires photoanode with tuning surface state via bottom-up interfacial engineering. Energy Environ Sci. 2017;10:2124–36. https://doi.org/10.1039/C7EE01475A.

98. Heaney MB. Electrical conductivity and resistivity. In: Webster JG, editor. Electrical measurement, signal processing, and displays. CRC Press; 2003. p. 7-1-7–14. https://doi.org/10.1201/9780203009406.

99. Chen D, Liu Z, Zhou M, Wu P, Wei J. Enhanced photoelectrochemical water splitting performance of α-Fe2O3 nanostructures modified with Sb2S3 and cobalt phosphate. J Alloys Compd. 2018;742:918–27. https://doi.org/10.1016/j.jallcom.2018.01.334.

100. Vilanova A, Lopes T, Spenke C, Wullenkord M, Mendes A. Optimized photoelectrochemical tandem cell for solar water splitting. Energy Storage Mater. 2017;13:175–88. https://doi.org/10.1016/j.ensm.2017.12.017.

101. Landman A, Halabi R, Dias P, Dotan H, Mehlmann A, Shter GE, Halabi M, Naseraldeen O, Mendes A, Grader GS, Rothschild A. Decoupled photoelectrochemical water splitting system for centralized hydrogen production. Joule. 2020;4:448–71. https://doi.org/10.1016/j.joule.2019.12.006.

102. Gurudayal D, Sabba HK, Mulmudi LH, Wong J, Barber M, Grätzel N. Mathews perovskite-hematite tandem cells for efficient overall solar driven water splitting. NANO Lett. 2015;15:3833–9.

103. Gurudayal A, John PP, Boix C, Yi C, Shi MC, Scott SA, Veldhuis AM, Minor SM, Zakeeruddin H, Wong M, Grätzel N. Mathews atomically altered hematite for highly efficient perovskite tandem water-splitting devices. Chem Sus Chem. 2017;10:2449–56. https://doi.org/10.1002/cssc.201700159.

104. Yu Z, Perera IR, Daeneke T, Makuta S, Tachibana Y, Jasieniak JJ, Mishra A, Bäuerle P, Spiccia L, Bach U. Indium tin oxide as a semiconductor material in efficient p-type dye-sensitized solar cells. NPG Asia Mater. 2016;8: e305. https://doi.org/10.1038/am.2016.89.

105. Nicolescu M, Mitrea D, Hornoiu C, Preda S, Stroescu H, Anastasescu M, Calderon-Moreno JM, Predoana L, Teodorescu VS, Maraloiu VA, Zaharescu M, Gartner M. Structural optical, and sensing properties of Nb-doped ITO thin films deposited by the sol-gel. Method, Gels. 2022;8:717. https://doi.org/10.3390/gels8110717.

106. Attia A, El-sadek MSA, Elnobi S, Soga T. Effect of transparent conducting substrates on the structure and optical properties of tin (II) oxide (SnO) thin films: comparative study. Ceram Int. 2021;47:13510–8. https://doi.org/10.1016/j.ceramint.2021.01.209.

107. Hakeem AMA, Ali HM, El-Raheem MMA, Hasaneen MF. Study the effect of type of substrates on the microstructure and optical properties of CdTe Thin Films. Opt Int J Light Electron Opt. 2020;225: 165390. https://doi.org/10.1016/j.ijleo.2020.165390.

108. Riha SC, Vermeer MJD, Pellin MJ, Hupp JT, Martinson ABF. Hematite-based photo-oxidation of water using transparent distributed current collectors. ACS Appl Mater Interfaces. 2013;5:360–7. https://doi.org/10.1021/am302356k.

109. Kaouk A, Ruoko T-P, Pyeon M, Gönüllü Y, Kaunisto K, Lemmetyinen HJ, Mathur S. High water-splitting efficiency through intentional in and Sn co-doping in hematite photoanodes. J Phys Chem C. 2016;120:28345–53. https://doi.org/10.1021/acs.jpcc.6b10432.

110. Zandi O, Beardslee JA, Hamann T. Substrate dependent water splitting with ultrathin α-Fe2O3 electrodes. J Phys Chem C. 2014;118:16494–503. https://doi.org/10.1021/jp4116657.

111. He X, Tian W, Yang L, Bai Z, Li L. Optical and electrical modulation strategies of photoelectrodes for photoelectrochemical water splitting. Small Methods. 2023;8:2300350. https://doi.org/10.1002/smtd.202300350.

112. Yu Q, Meng X, Shi L, Liu G, Li P, Ye J. Hematite homojunctions without foreign element doping for efficient and stable overall water splitting. RSC Adv. 2016;6:62263–9. https://doi.org/10.1039/C6RA13060G.

113. Piekner Y, Ellis DS, Grave DA, Tsyganok A, Rothschild A. Environmental Science Wasted photons: photogeneration yield and charge carrier collection efficiency of hematite photoanodes for photoelectrochemical water splitting. Energy Environ Sci. 2021;14:4584–98. https://doi.org/10.1039/d1ee01772a.

114. Wang KX, Yu Z, Liu V, Brongersma ML, Jaramillo TF, Fan S. Nearly total solar absorption in ultrathin nanostructured iron oxide for efficient photoelectrochemical water splitting. ACS Photonics. 2014;1:235–40. https://doi.org/10.1021/ph4001026.

115. Iandolo B, Zhang H, Wickman B, Zori I, Conibeer G, Hellman A. Correlating flat band and onset potentials for solar water splitting on model hematite photoanodes. RSC Adv. 2015;5:61021–30. https://doi.org/10.1039/c5ra10215d.

116. Jiang D, Yue Q, Tang S, Zhang L, Zhu L, Du P. A highly efficient photoelectrochemical cell using cobalt phosphide-modified nanoporous hematite photoanode for solar-driven water splitting. J Catal. 2018;366:275–81. https://doi.org/10.1016/j.jcat.2018.07.037.

117. Kaur G, Divya, Khan SA, Satsangi VR, Dass S, Shrivastav R. Nano-hetero-structured thin films, ZnO/Ag-(a)Fe2O3, with n/n junction, as efficient photoanode for renewable hydrogen generation via photoelectrochemical water splitting. Renew Energy. 2021;164:156–70. https://doi.org/10.1016/j.renene.2020.09.060.

118. Kodan N, Agarwal K, Mehta BR. All-oxide α-Fe2O3/H:TiO2 heterojunction photoanode: a platform for stable and enhanced photoelectrochemical performance through favorable band edge alignment. J Phys Chem C. 2019;123:3326–35. https://doi.org/10.1021/acs.jpcc.8b10794.

119. Palmolahti L, Ali-Loytty H, Khan R, Saari J, Tkachenko NV, Valden M. Modification of surface states of hematite-based photoanodes by submonolayer of TiO2 for enhanced solar water splitting. J Phys Chem C. 2020;124:13094–101. https://doi.org/10.1021/acs.jpcc.0c00798.

120. Ikrama A, Islama S, Zulfequar M. Visible light driven Cu2ZnSnS4 QDs/α-Fe2O3 -Graphene heterojunction for photoelectrochemical water splitting. SSRN. 2022;1:1–18.

121. Yu Q, Meng X, Wang T, Li P, Ye J. Hematite films decorated with nanostructured ferric oxyhydroxide as photoanodes for efficient and stable photoelectrochemical water splitting. Adv Funct Mater. 2015;25:2686–92. https://doi.org/10.1002/adfm.201500383.

122. Elishav O, Stone D, Tsyganok A, Jayanthi S, Ellis DS, Yeshurun T, Maor II, Levi A, Beilin V, Shter GE, Yerushalmi R, Rothschild A, Banin U, Grader GS. Composite indium tin oxide nanofibers with embedded hematite nanoparticles for photoelectrochemical water splitting. ACS Appl Mater Interfaces. 2022;14:41851–60. https://doi.org/10.1021/acsami.2c05424.

123. Urbain F, Tang P, Smirnov V, Welter K, Andreu T, Finger F, Arbiol J, Morante JR. Insights into the combination of multilayered hematite nanowires with thin-film silicon photovoltaics in an all-earth-abundant hybrid tandem device for solar water splitting. Chem Sus Chem. 2019;12:1–17. https://doi.org/10.1002/cssc.201802845.

124. Koziol-Rachwal A, Kwiatek N, Skowronski W, Grochot K, Kanak J, Madej E, Freindl K, Korecki J, Spiridis N. Insight into the structural and magnetotransport properties of epitaxial α-Fe2O3/Pt (111) heterostructures: role of the reversed layer sequence. Phys Rev B. 2022;106:104419. https://doi.org/10.1103/PhysRevB.106.104419.

125. Wang L, Yang Y, Zhang Y, Rui Q, Zhang B, Shen Z, Bi Y. One dimensional Hematite photoanodes with spatially separated Pt and FeOOH nanolayers for efficient solar water splitting. J Mater Chem A. 2017;5:17056–63. https://doi.org/10.1039/C7TA05318E.

126. Baldovi HG. Optimization of α-Fe2O3 nanopillars diameters for photoelectrochemical enhancement of α-Fe2O3-TiO2 heterojunction. Nanomaterials. 2021;11:1–16. https://doi.org/10.3390/nano11082019.

127. Bondarchuk AN, Corrales-Mendoza I, Tomas SA, Marken F. A hematite photoelectrode grown on porous and conductive SnO2 ceramics for solar-driven water splitting. Sci Direct Int J Hydrog Energy. 2019;44:19667–75. https://doi.org/10.1016/j.ijhydene.2019.06.055.

128. Papageorgiou N. Counter-electrode function in nanocrystalline photoelectrochemical cell configurations. Coord Chem Rev. 2004;248:1421–46. https://doi.org/10.1016/j.ccr.2004.03.028.

129. Andrade L, Lopes T, Ribeiro HA, Mendes A. Transient phenomenological modeling of photoelectrochemical cells for water splitting e Application to undoped hematite electrodes. Int J Hydrogen Energy. 2011;36:175–88. https://doi.org/10.1016/j.ijhydene.2010.09.098.

Discover